8-2016

Ultrasound and photoacoustic methods for anatomic and functional imaging in image guided radiation therapy

Justin T. Sick
Purdue University

Graduate School Form
30 Updated 12/26/2015

PURDUE UNIVERSITY
GRADUATE SCHOOL
Thesis/Dissertation Acceptance

This is to certify that the thesis/dissertation prepared

By Justin T Sick

Entitled

UTRASOUND AND PHOTOACOUSTIC METHODS FOR ANATOMIC AND FUNCTIONAL IMAGING IN IMAGE GUIDED RADIATION THERAPY

For the degree of Doctor of Philosophy

Is approved by the final examining committee:

Keith Stantz
Chair

Jeannie Poulson

Deborah Knapp

Colleen DesRosiers

To the best of my knowledge and as understood by the student in the Thesis/Dissertation Agreement, Publication Delay, and Certification Disclaimer (Graduate School Form 32), this thesis/dissertation adheres to the provisions of Purdue University's "Policy of Integrity in Research" and the use of copyright material.

Approved by Major Professor(s): Keith Stantz

Approved by: Shuang Liu

Head of the Departmental Graduate Program Date

ULTRASOUND AND PHOTOACOUSTIC METHODS FOR ANATOMIC AND FUNCTIONAL IMAGING IN IMAGE GUIDED RADIATION THERAPY

A Dissertation

Submitted to the Faculty

of

Purdue University

by

Justin T Sick

In Partial Fulfillment of the

Requirements for the Degree

of

Doctor of Philosophy

August 2016

Purdue University

West Lafayette, Indiana

Dedicated to my parents

ACKNOWLEDGEMENTS

First, I would like to thank Dr. Keith Stantz for his unwavering support, guidance and expertise that made this work possible. Additionally, I would like to thank my committee members: Dr. Jeannie Poulson, Dr. Deborah Knapp and Dr. Colleen DesRosiers for all of their contributions.

So much of this work was made possible by the Purdue University Veterinary Teaching Hospital, specifically, the department of Radiation Oncology and the department of Radiology. I am honored to have worked with the brilliant faculty and staff in such a wonderful hospital.

Finally, the completion of this document would not have been possible without the love and support from my parents, Thomas and Karen Sick, family, friends and loved ones. I could not have done it without you.

TABLE OF CONTENTS

Page

Page

LIST OF TABLES

LIST OF FIGURES

Appendix Figure Page

ABSTRACT

Sick, Justin T. Ph.D., Purdue University, August 2016. Ultrasound and Photoacoustic Methods for Anatomic and Functional Imaging in Image Guided Radiation Therapy. Major Professor: Keith Stantz.

(PURPOSE) The goal of this research is to develop image-guided radiotherapy techniques based on ultrasound and photoacoustic instrumentation and methods.

(INTRODUCTION) A critical problem in RT is the intra and inter-fractional changes in the target geometry, positioning, and biology, which can impact tumor control and systemic toxicity. Unlike other imaging modalities, ultrasonic-based imaging techniques provides real-time, high resolution imaging of a patient's anatomy and tumor physiology and hypoxia without the use of ionizing radiation. In the following studies, technical studies are performed to integrate 3D ultrasound into the IMRT treatment planning of dogs with bladder cancer, in effect, replacing CBCT, and feasibility studies performed to determine if photoacoustic imaging can be used to monitor changes in oxygen saturation levels.

(MATERIAL and METHODS) First, we define the physical principals and optimal protocols that provide contrast when imaging with US and the transducer properties contributing to resolution limits. The US field of view (FOV) was

characterized to determine the optimal settings with regard to imaging depth, focal region, with and without harmonic imaging, and artifact identification. This will allow us to determine the minimum errors expected when registering multimodal volumes (CT, US, CBCT).

Next, we designed an in-house integrated US manipulator and platform to relate CT, 3D-US and linear accelerator coordinate systems. To validate our platform, an agar-based phantom with measured densities and speed-of-sound consistent with tissues surrounding the bladder was fabricated. This phantom was rotated relative to the CT and US coordinate systems and imaged with both modalities. These CT and 3D-US images were imported into the treatment planning system, where US-to-US and US-to-CT images were co-registered and the registration matrix used to re-align the phantom relative to the linear accelerator. The measured precision in the phantom setup, which is defined by the standard deviation of the transformation matrix components, was consistent with and exceeding acceptable clinical patient re-alignments (2 mm). Statistical errors from US-US registrations for different patient orientations ranged from 0.06-1.66 mm for x, y, and z translational components, and 0.00-1.05 degrees for rotational components. Statistical errors from US-CT registrations were 0.23-1.18 mm for the x, y and z translational components, and 0.08-2.52 degrees for the rotational components. The high precision in the multimodal registrations suggest the ability to use US for patient positioning when targeting abdominal structures. We are now testing this on a dog patient to obtain both inter and intra-fractional positional errors.

The objective of this experiment is to confirm Hill's equation describing the relationship between hemoglobin saturation (SaO_2) and the partial pressure of dissolved

oxygen (pO_2). The relationship is modeled as a sigmoidal curve that is a function of two parameters – the Hill coefficient, n, and the net association constant of HbO_2, K (or pO_2 at 50% SaO_2). The goal is to noninvasively measure SaO_2 in breast tumors in mice using photoacoustic computed tomographic (PCT) imaging and compare those measurements to a gold standard for pO_2 using the OxyLite probe. First, a calibration study was performed to measure the SaO_2 (co-oximeter) and pO_2 (Oxylite probe) in blood using Hill's equation (P50=23.2 mmHg and n=2.26). Next, non-invasive localized measurements of SaO_2 in MDA-MD-231 and MCF7 breast tumors using PCT spectroscopic methods were compared to pO_2 levels using Oxylite probe. The fitted results for MCF7 and MDA-MD-231 data resulted in a P50 of 17.2 mmHg and 20.7 mmHg and a n of 1.76 and 1.63, respectively. The lower value of the P50 is consistent with tumors being more acidic than healthy tissue. Current work applying photon fluence corrections and image artifact reduction is expected to improve the quality of the results. In summary, this study demonstrates that photoacoustic imaging can be used to monitor tumor oxygenation, and its potential use to investigate the effectiveness of radiation therapy and the ability to adapt therapeutic protocols.

CHAPTER 1. INTRODUCTION

1.1 Advantages of the Canine Model

New animal models better representing invasive bladder cancer in humans are needed before translating experimental treatments from the laboratory into the clinic[1]. Spontaneous invasive transitional cell carcinoma (TCC) is the most common cancer of the canine urinary system and is only partially responsive to treatment with surgical resection or systemic chemotherapy. Radiation therapy (RT) is made technically difficult by the considerable internal variations in bladder size, shape and position[2]. The advantages of canine model systems were described previously[1] and have been applied to TCC. Knapp, et al.[3] offered some of these benefits which include: 1) similarities in histopathologic appearance, biological behavior and response to therapy in both canine cancer and human cancer, 2) dogs and humans have similar drug metabolism, 3) standard treatments are less defined for many canine cancers, therefore fewer constraints are placed on testing new therapies, 4) the compressed lifespan of canines makes for shorter clinical trials, 5) canines have similar exposures to toxins as humans due to shared living space, 6) testing translatable technologies is more feasible on animals closer to the size of humans, and 7) novel interventional strategies established *in vitro* or in laboratory animal studies can be verified *in vivo* in spontaneous tumor-bearing dogs. The investigation of

spontaneous cancer is also more tolerable to a general public worried about animal welfare than inducing disease in animals for examination.

1.2 Radiation Therapy

The use of radiation to target cancer was recognized early after the discovery of x-rays[4]. Rapid advancements in accelerator technology have made feasible the delivery of x-rays to tumor volumes in addition to reducing accumulative healthy tissue dose. Improvement of RT progressed quickly during the 20th and 21st centuries, starting with 3D conformal radiation therapy (CRT), to intensity modulated radiation therapy (IMRT), to stereotactic radiosurgery (SRS) and more recently, tomotherapy. Developments in high-quality imaging systems are necessary to deliver more conformal RT.

Where early therapy sessions included a single pre-treatment CT for simulation, new advancements have allowed for constant monitoring of patient anatomy throughout the treatment process. The method of frequent two and three-dimensional imaging throughout a course of radiation treatment used to direct RT is termed image-guided radiation therapy (IGRT). Radiation treatment incorporating any number of imaging modalities to systematically modify the treatment plan is termed ‘adaptive radiation therapy’ (ART). Image-guided adaptive radiotherapy (IGART) has the possibility to lessen the adverse effects from inter- and intra-fractional geometric and biologic fluctuations. There are three phases during the sequence of the radiotherapy process where imaging is used: 1) patient data acquisition; 2) patient setup for treatment; 3) during treatment to monitor organ motion.

1.3 Standard IGRT imaging techniques

The specialized improvement of imaging hardware and software intended to visualize internal anatomy during treatment has become an area of active research[5,6]. The typical IGRT technologies include kilovoltage (kV) and megavoltage (MV) portal and radiographic imaging systems and in-room computed tomography (CT).

Electronic portal imaging has been the preferred tool for online verification of patient setup in the past decades[7]. Portal imaging is the acquisition of images with the treatment beam; typically two or more directions are acquired before the delivery of radiation[8]. The portal images are compared to digitally reconstructed radiographs to ensure the patient is in the ideal setup position. In sites where there is little tumor motion with respect to the bony anatomy, such as the head and neck, the bones can be used for the reference. For treatment locations where organ motion is significant, fiducial markers implanted in the tumor volume or near it can be seen on the portal images and used as the reference. Although the kV images have better contrast than the MV images, neither of them is of sufficient quality to visualize soft-tissue targets in their entirety. Additionally, they typically require independent X-ray sources and detectors, consequently introducing an element of uncertainty between the imaging and beam iso-centers as well as an additional cost to therapy centers.

The widespread availability CT in the field of radiation oncology makes daily visualization and localization of soft tissue anatomy in the therapy suite prior to delivery of treatment commonplace. These advancements have highlighted the ability to improve treatment accuracy with respect to patient positioning. A number of types of in-room CT imaging systems are now available. A few examples include a ‘CT on rails’ system

consisting of a conventional CT scanner located in the treatment vault on the same couch as the linear accelerator, kV cone-beam CT (CBCT) composed of an additional diagnostic kV source and a flat-panel detector mounted orthogonally to the treatment head and MV CBCT systems using the pre-existing treatment machine and an electronic portal imaging device[9].

1.4 Managing imaging dose

Image-guided RT makes use of a variety of different radiographic modalities to monitor patient position and organ motion. All radiographic guidance techniques share the fact that they can give a considerable radiation dose to the patient. As a result, the American Association of Physicists in Medicine assigned a task group to determine guidelines for managing imaging dose[9]. This report concluded that as a result of the many different imaging techniques used in IGRT, including different modalities (portal imaging, fluoroscopy, kV and MV-CBCT and multiple conventional CT scans) as well as the various time frames the dose is received by the patient (weeks for conventional RT, days for hypo-fractionated RT and radiosurgery), it is not accurate to assume the cumulative imaging dose is trivial when compared to the therapeutic dose.

1.5 In-vivo molecular imaging

In-vivo models including complete physiologic processes such as multiple organ interactions, angiogenesis and the immune system are necessary to improve current in-vitro models[3]. Dynamic contrast-enhanced CT (DCE-CT), dynamic contrast enhanced magnetic resonance imaging (MRI) (DCE-MRI), positron emission tomography (PET)

and single-photon emission tomography (SPECT) have been extensively used for in vivo measurement of tumor vascular physiology[10,11].

PET and SPECT imaging monitor an injectable radioisotope tracer to evaluate function, such as metabolic activity using 18-FDG, and a CT scan to provide spatial information about the tracer uptake. PET/CT is a promising diagnostic innovation and is the standard of care monitoring modality in human malignancies. Unfortunately, there are many disadvantages to the use of PET/CT. Patients, staff, family members and the general public are potentially exposed to these radioactive isotopes. The amount of ionizing radiation involved is non-trivial and especially concerning when the diagnostic intervention is proposed for at-risk populations of cancer patients such as children.

Instead, photoacoustic tomography (PAT) is a nonionizing and noninvasive imaging modality employing laser-induced ultrasonic signals within biological tissue. This imaging method merges the high resolution of ultrasonic signals with the contrast being provided by optical scattering and absorption. This allows for non-invasive structural and functional imaging in-vivo[12].

1.6 Therapeutic targets

Ionizing radiations stimulates both pro- and anti-proliferative signal pathways generating an imbalance in cell survival decision controlled by a number of genes and factors involved in cell cycle progression, survival and/or cell death, DNA repair and inflammation[13]. The body's reaction to cancer resembles inflammation and wound healing[14]. The idea of the immune system identifying and targeting mutated cells as a result of a particular immune reaction to the tumor, causing inflammation, is

demonstrated by recent evidence[15]. Alternatively, inflammation promotes the release of pro-inflammatory cytokines, some of which may stimulate tumor progression[16]. The most likely scenario is that tumor-promoting inflammation and anti-tumor immunity co-exist during the course of tumor progression and conditions in the tumor environment influence the balance between the two[17].

Assessment of the molecular and functional features of tumors may allow the characterization of local weaknesses that can be exploited to focus treatment strategies. Although tumor masses regularly appear homogeneous on CT scans, this is rarely the case. Heterogeneity in viable and necrotic tissue, angiogenesis and anoxia, rate of cellular growth and cell death, as well as receptor and antigen expression frequently go undetected[18]. Various signals that control angiogenesis include low partial oxygen pressure (pO_2), low pH or hypoglycemia as a consequence of metabolic trauma, increased pressure in the stroma due to proliferating cells, an immune/inflammatory response and genetic mutations[19]. All of these features are very important in determining the stage and therapeutic resistance of the tumor and in principle, assessing these features could be extremely helpful for developing new treatment strategies.

1.7 Hypothesis

The purpose of IGRT is to track organ motion in real-time to monitor treatment uncertainties. In general, these uncertainties all into two categories physical and physiological, and they manifest themselves in margins expanded from the tumor volume. The underlying problem with this procedure is planning to give the healthy surrounding tissue a lethal dose to ensure tumor control, especially when the limiting

factor of RT is healthy tissue toxicity. Therefore, incorporating imaging systems to reduce planning margins will limit radiation induced side effects. Additionally, visualizing the heterogeneity of the tumor and planning treatments to apply focused daily boosts of radiation and re-evaluating conventional fractionation will increase the therapeutic ratio of the dose being delivered, and in turn, improve tumor control.

Our goal is two-fold: 1) to accurately track the bladder during RT of canine TCC through daily 3D transabdominal US and 2) to concurrently image intra-tumor variations in hypoxia in these same patients. With these tools, both geometric and molecular features can be monitored in real-time and used to investigate and adapt radiation therapy in these patients. Therefore, the goal of this research is to develop image-guided radiotherapy techniques based on ultrasound (US) and photoacoustic (PA) instrumentation and methods.

CHAPTER 2. SPECIFIC AIMS

2.1 Specific Aim 1

Quantify the resolution of 3D US imaging systems. The purpose of this section is to define the physics that provides contrast when imaging with US and the transducer properties contributing to resolution limits. Next, the US field of view (FOV) will be characterized to determine the optimal settings with regard to imaging depth, focal region, with and without harmonic imaging, and artifact identification. This information will provide a basis from which to compare our phantom studies in the studies to volume, including the minimum errors expected when registering multimodal volumes (CT, US, CBCT).

2.2 Specific Aim 2

Design, construct and commission a platform for US imaging in combination with CT. The platform provides a reproducible positional frame of reference for targeting an anatomic structure. The platform will interlock with Varian exact couch index points and CT diagnostic scanner for reproducibility of positioning. The platform will be imaged for all discrete positions (via CT scanner), where discrete angles will be measured and saved within a MATLAB^{TM} graphical user interface (GUI). The platform will be calibrated to the coordinate system of

the linear accelerator. Our objective is to obtain CT and US alignment errors within or better than cone-beam computed tomography (CBCT), which is ±2mm.

Given the translational validation of the US for clinical treatment of canine patients, our focus is toward the feasibility of using PCT to provide new imaging properties and link this to tumor radiation sensitivity and immune response of the patient.

2.3 Specific Aim 3

Validate hemoglobin saturation and dissolved oxygen in tumors using photoacoustic spectroscopic imaging. This pilot study investigates the method to measure SaO2 levels in mice and examines the feasibility to translate photoacoustic tomographic imaging in to a canine model. First, a calibration study to validate Hill's equation in blood will be performed by creating a closed circuit blood-flow phantom to test the relationship between SaO_2 (co-oximeter) and pO_2 (Oxylite probe). Next, non-invasive localized measurements of SaO_2 in MDA-MD-231 and MCF7 breast tumors using PCT spectroscopic methods will be compared to pO_2 levels (Oxylite probe) in vivo. Finally, the design concept of photoacoustic tomographic imaging in a canine model will be explored.

2.4 Innovation and Impact

By using real-time motion tracking through US-based anatomical information and PA molecular imaging, treatment margins can be reduced, which will improve tumor control and reduce normal tissue radiation toxicity. The proposed innovative design combines 3-D US and PA imaging in a single system that can be integrated onto RT

treatment bed. The whole system, minus the transducer, will be primarily fabricated using 3D printing techniques using low Z material so it is not to interfere with CT simulation and RT. The US imaging will provide real-time images without the use of ionizing radiation. We anticipate PA imaging will impact RT in two ways: 1) it will increase the accuracy when delineating the tumor margins by identifying the vasculature at the periphery of the tumor, and 2) provide the means to characterize the tumor with spatial and molecular information in the tumor and normal structures. The day-to day (inter- and potential intra-fraction) information afforded by US and PA images will allow for adaptive radiotherapy treatment planning based on molecular and functional imaging - such as hypoxia (via SaO2) and perfusion (contrast-enhanced PCT; microbubble enhanced US), cytokine production, and potentially hypoxic type (cycling versus chronic).

CHAPTER 3. QUANTIFY THE RESOLUTION OF 3D US IMAGING SYSTEMS

3.1 Introduction

The method of frequent two and three-dimensional imaging throughout a course of radiation treatment used to direct RT is termed image-guided radiation therapy (IGRT). In essence, imaging devices are used by the radiation therapy team as tools to verify patient setup and provide a means for the safe delivery of treatment. The standard for simulation and treatment planning is computed tomography (CT) to obtain anatomical electron distributions followed by cone-beam computed tomography (CBCT) to verify or align the patient on the IMRT bed. The treatment volume (CBCT) is often registered to the simulation volume (CT) to determine the appropriate daily treatment couch shifts. The registered volumes allow the radiation oncology team to position the patient as close as possible to the simulated treatment orientation. One problem with CBCT is that the imaging procedure is done right before treatment delivery, thus it cannot monitor patient and organ motion during treatment to determine if the target has moved out of the treatment field.

Ultrasound (US) offers an attractive alternative to CBCT for imaging IGRT targets in the abdomen, such as the bladder. US-based guidance systems can provide intrafractional motion with high spatial and temporal resolution. The

purpose of this chapter is to define the physics that provides contrast when imaging with US and the transducer properties contributing to resolution limits. Next, the US field of view (FOV) will be characterized to determine the optimal settings with regard to imaging depth, focal region, with and without harmonic imaging, and artifact identification. Defining the optimal imaging parameters will allow us to determine the minimum errors expected when registering multimodal volumes.

3.2 Ultrasound Imaging

3.2.1 Wave propagation

Mechanical energy transmits through a continuous, elastic medium by the compression and rarefaction of "particles" that comprise it[20]. The waves travel at a speed of sound c, given by,

$$c = \sqrt{\frac{1}{\kappa\rho}} \tag{3.1}$$

Where κ is the compressibility and ρ is the density of the material.

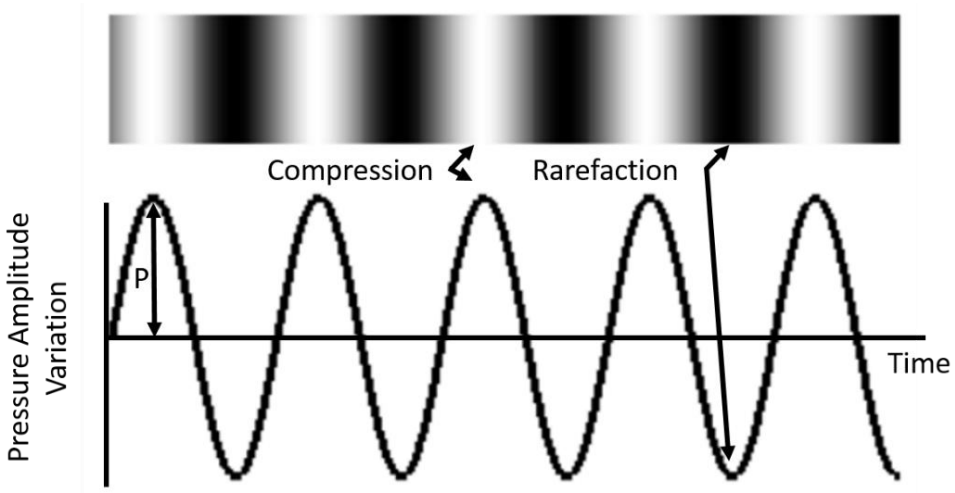

Figure 3.1 Ultrasound wave propagation. Ultrasound energy is generated by a mechanical displacement in compressible medium. Energy propagation is shown as a function of time, resulting in areas of compression and rarefaction with corresponding variations in positive and negative pressure amplitude.

The waves are three-dimensional and dependent on time. Independent of the physical measures used to describe sound waves, they must depend on three variables in the spatial domain, x, y and z, and time, t[21]. The particles are displaced from equilibrium by a displacement amplitude, u(x, y, z, t), and at a particle velocity, v(x, y, z, t)), as the wave disturbance passes through the medium. This change also corresponds to a local pressure disturbance, p(x, y, z, t), that must satisfy the three-dimensional wave equation,

$$\left(\frac{\partial^2}{\partial x^2}+\frac{\partial^2}{\partial y^2}+\frac{\partial^2}{\partial z^2}\right)p(x,y,z,t)=\frac{1}{c^2}\frac{\partial^2 p(x,y,z,t)}{\partial t^2} \tag{3.2}$$

If we assume a plane wave traveling in the z-direction, the wave equation reduces to,

$$\frac{\partial^2 p(z,t)}{\partial z^2}=\frac{1}{c^2}\frac{\partial^2 p(z,t)}{\partial t^2} \tag{3.3}$$

with the solution to the particle's position at any given time,

$$u(z,t)=\mathrm{A}\sin(kz-\omega t) \tag{3.4}$$

where A is the maximum displacement, k is defined as the wavenumber, $k=\frac{\omega}{c}$, and ω is the angular frequency, $\omega=2\pi f$.

The driving force of a wave in matter is the pressure and the particle velocity[22]. Therefore, the characteristics of a sound wave relates to the properties of the medium in which it is propagating by the acoustic impedance, Z, which is the ratio of the pressure to particle velocity[22].

$$Z\equiv\frac{p(z,t)}{v(z,t)} \tag{3.5}$$

where,

$$p(z,t)=-\frac{1}{\kappa}\frac{\partial s}{\partial z}=-\frac{1}{\kappa}\frac{\partial[Asin(kz-\omega t)]}{\partial z}=-\frac{1}{\kappa}Akcos(kx-\omega t) \tag{3.6}$$

and,

$$v(z,t) = \frac{\partial u}{\partial t} = \frac{\partial [A sin(kz - \omega t)]}{\partial t} = -A\omega \cos(kz - \omega t) \tag{3.7}$$

Therefore,

$$Z = \frac{-\frac{1}{\kappa} Ak cos(kx - \omega t)}{-A\omega \cos(kz - \omega t)} \tag{3.8}$$

where the relationships,

$$\kappa = \frac{1}{\rho c^2}\ , k = \frac{\omega}{c} \tag{3.9}$$

can be used to reduce Z to,

$$Z = \rho c \tag{3.10}$$

3.2.2 Interactions with Matter

As the pressure waves travel through the medium, they experience a number of interactions, where the primary interaction resulting in US contrast is the scattering properties. If the boundary is large compared to the wavelength, specular reflections dominate, where the transmitted portion of the wave will bend or refract as the angle of incident of the acoustic wave relative to the boundary deviates from being perpendicular. Non-specular acoustic scattering arises from objects that are the size of the wavelength or smaller, resulting in diffuse reflections

If a perpendicular wave travels from a material of acoustic impedance, Z_1, to a material of acoustic impedance, Z_2, a fraction of the sound intensity is reflected. The reflection coefficient, R_I, describes the ratio of the intensity of the wave that is reflected to the intensity of the incident wave.

$$R_I = \left(\frac{Z_2 - Z_1}{Z_2 + Z_1}\right)^2 \tag{3.11}$$

The fraction that is transmitted is,

$$T_I = 1 - R_I \tag{3.12}$$

If the wave is not normal to the boundary, the transmitted wave bends according to Snell's Law,

$$\frac{\sin(\theta_t)}{\sin(\theta_i)} = \frac{c_2}{c_1}, \tag{3.13}$$

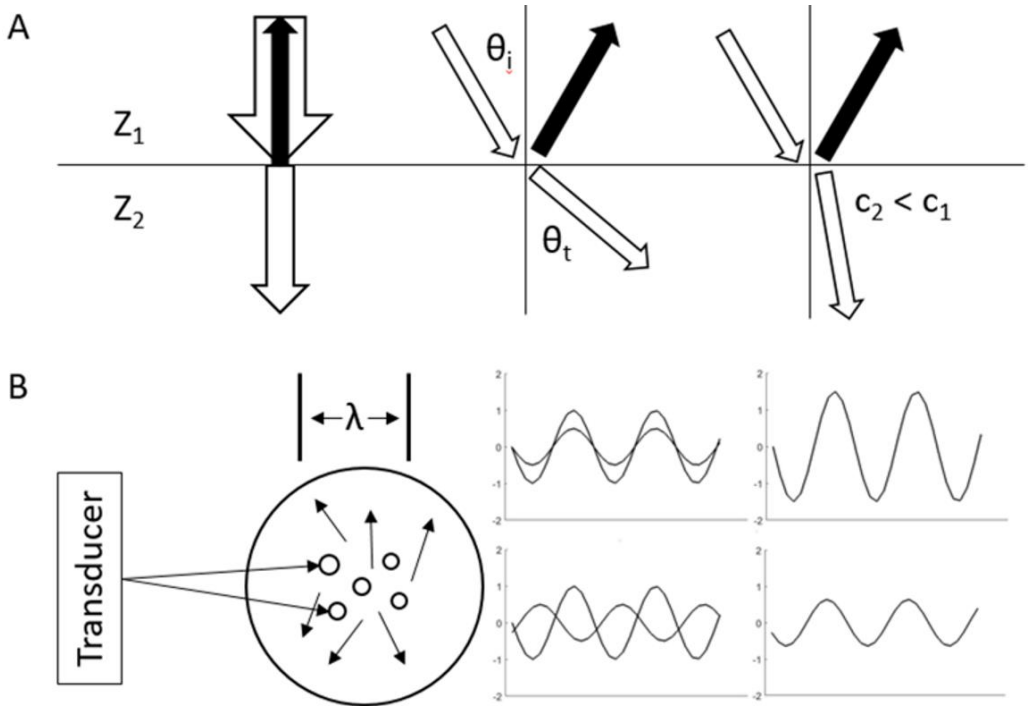

Figure 3.2 Ultrasound interactions with matter. A) Reflection and refraction of ultrasound occur at tissue boundaries with difference in acoustic impedance, Z. From left to right: Perpendicular incidence (90 degrees), non-perpendicular incidence ($c_2 > c_1$), non-perpendicular incidence ($c_2 < c_1$). B) Specular scattering (left), Constructive and destructive interference of scattered waves (right).

3.2.3 Beam Formation

Ultrasound waves are produced and detected with a transducer, comprised of one or more ceramic elements (piezoelectric) with electromechanical properties and peripheral components[20]. When voltage is applied to the elements, the crystals change their structure, causing the elements to expand and contract. This physical deformation converts electrical energy into mechanical energy, generating sound waves. Inversely, mechanical pressure administered to the surface of the crystal produces electrical energy. Transducers used for standard pulse-echo ultrasound imaging operate in a "resonance" mode, whereby a short voltage pulse is applied, triggering the piezoelectric element to contract and then vibrate at a natural resonance frequency[20]. A damping block is positioned on the back of the piezoelectric element, to produce an ultrasound pulse with a short spatial pulse length (SPL). Dampening of the vibration introduces a broadband frequency spectrum. The "Q factor" describes the bandwidth of the sound emanating from the transducer as

$$Q = \frac{f_0}{Bandwidth} \tag{3.14}$$

A narrow bandwidth and long SPL are observed in" high Q" transducers whereas wide bandwidths and short SPLs are the result of "low Q" transducers[20].

3.2.4 Resolution

As the ultrasound beam propagates from the transducer surface into the medium, it displays two unique beam patterns. The near field is before a distance determined by the geometry and frequency of the transducer where the beam converges. Beam convergence in the near field happens because of various constructive and destructive

interference patterns of the waves produced from the transducer surface. The beam diverges in the Fraunhofer (far field) zone and in contrast to the near field, intensity decreases with distance.

The ability of an US system to discern two objects in space, the axial and lateral resolution, is primarily dependent on the transducer properties. The axial resolution is along the direction of the beam and is independent of depth. The SPL limits the axial resolution. Reflectors that are separated by a distance greater than ½ the SPL produce echoes from the first object that are completely distinct from echoes reflected from the second object, whereas boundaries with less than ½ the SPL result in returning echoes not being able to be resolved[20]. Higher frequencies reduce the SPL and thus improve the axial resolution. Lateral resolution is defined as the capability to distinguish two separate objects in close proximity perpendicular to the beam direction. Lateral resolution depends on depth, beam frequency and scan line density[23]. The highest lateral resolution is found at the focal distance and adequate in the focal zone.

3.2.5 Artifacts

Image quality is dependent on the design characteristics of the ultrasound equipment, the numerous equipment variables selected, and positioning skills of the operator. Image quality is measured by spatial resolution, contrast to noise and image uniformity. Image artifacts are common in ultrasound and often degrade image quality, although on occasion they can be used to enhance diagnostic integrity. Artifacts are the inaccurate display of anatomy during image acquisition. The causes are variations in

operator technique, machine degradation or simply inherent to ultrasound interaction with tissues.

Common artifacts include reverberation, refraction, shading and enhancement, speed displacement, and speckle. Reverberation appears as the inaccurate display of tissues due to signals being reflected back and forth between two closely spaced objects or interfaces[24]. Refraction is a change in the longitudinally transmitted ultrasound direction at a boundary where the angle of incidence deviates from being perpendicular between two tissues with differing speed-of-sounds (seen in Figure 3.2). Shadowing is a weak signal beyond an object or interface. It is caused by objects with high attenuation coefficients or reflection from large Z differences of the incident beam. Enhancement occurs beyond objects having low attenuation, for example, fluid-filled cavities (e.g. bladder). Hyperintense signals return the transducer not proportional to the assumed transmission through these structures. Speed of sound displacement is produced by the variations of speed of sound in different tissues. All of the factors contribute to image distortion and blurring of the target boundaries.

3.3 Methods

3.3.1 Imaging Protocols

B-mode ultrasonography of all phantoms was performed with a dedicated ultrasonography machine (Philips iU22 SonoCT system, Philips Ultrasound, Bothell, WA). A broadband volume curved array transducer (6-2 MHz) was utilized.

The Computerized Imaging Reference Systems (CIRS, Norfolk, VA) Model 040GSE Multi-Purpose, Multi-Tissue Ultrasound Phantom was used for characterizing the field of view for different imaging parameters. The phantom includes a group of wire targets that appear as bright dots or lines (depending on the orientation of the transducer) in the image. These targets are made from nylon monofilimanet with diameter of 0.8 and 1.0 mm and have an attenuation of 0.5dB. The different target groups utilized in this experiment are shown in Table 3.1.

We imaged the phantom with a maximum depth of 16, 10 and 5 cm and a focal region in the top third, middle third and bottom third for the 16 and 10 cm depths. Only one focal region was used for the 5 cm depth procedure. Volumes were recorded with and without harmonic imaging for each procedure, resulting in 14 independent scans. Images were optimized with the use of the i-scan function (automatically compensate for gain) prior to each recording. Voxel size was only dependent on the depth and irrespective of the focal depth, with or without harmonic imaging or the use of the i-scan function. Voxel sizes can be seen in Table 3.2.

Table 3.1. Phantom target characteristics

Wire Targets		
Material	Nylon monofilament	
	Vertical Distance Group	**Horizontal Distance Groups**
Number of targets	16	6 & 7
Diameter	100 µm	100 µm
Depth Range	1 -16 cm	4 & 9 cm
Distance between targets	10 mm	10 & 20 mm

Table 3.2. Volumes and voxel sizes for the corresponding imaging depth

Depth [cm]	**Volume Dimensions [row/col/slice]**	**Voxel Size [Axial/Lateral/Elevational] [mm]**
16	512/510/256	0.463/0.337/0.670
10	512/510/256	0.336/0.219/0.450
5	512/463/256	0.229/0.132/0.269

3.3.2 Phantom Analysis

The full width half max (FWHM) of each wire was calculated for each depth, focal region, and with and without harmonic imaging. The average and standard deviation of the FWHM were calculated for each focal region of the corresponding image with respect to maximum depth of the image and with and without harmonic imaging. First, the axial and lateral resolution within the one focal region of the 5 cm depth image was determined as a function of depth and horizontal position. Next, the axial and lateral resolution was analyzed with the focus in the near, mid and far fields. This data was used to determine the optimal imaging procedure. Lastly, the FWHM and voxel sizes under ideal conditions were compared to that of CT and CBCT to determine the minimum statistical error associated with multimodal volume registrations.

3.3.3 Artifact Analysis

A series of Transitional Cell Carcinoma (TCC) cases presented to the Purdue University Veterinary Teaching Hospital were examined for artifacts. The images were recorded with diagnostic intent and consequently should have minimal artifacts. Therefore, any artifacts present can be assumed to also be present in a scenario where US is used solely for patient positioning, where the purpose of the procedure is not to diagnose disease but simply to identify the margins and boundaries of critical organs. Any artifacts present shall be quantified and included in error analysis to determine the minimum statistical error associated with multimodal volume registrations.

3.4 Results

3.4.1 Phantom

The US QA phantom was imaged under 14 unique conditions, which depended on the maximum depth of the scan, focal region, and with and without harmonics. The FWHM of 100 μm nylon wires was used to determine both the axial and lateral resolution throughout the FOV.

The initial scan, shown in Figure 3.3, was with a maximum depth of 5 cm and used only one focal region. We saw no change in axial resolution as a function of depth within the focal region. In addition, we saw no change in lateral resolution as function of horizontal position. The axial FWHM was significantly lower ($p = 0.000545$) in the harmonic image (1.88 ± 0.16 mm) than that of the original (2.78 ± 0.22 mm). The lateral FWHM was significantly higher ($p = 0.0212$) in the harmonic image (1.55 ± 0.18 mm) than that of the original (1.29 ± 0.15 mm).

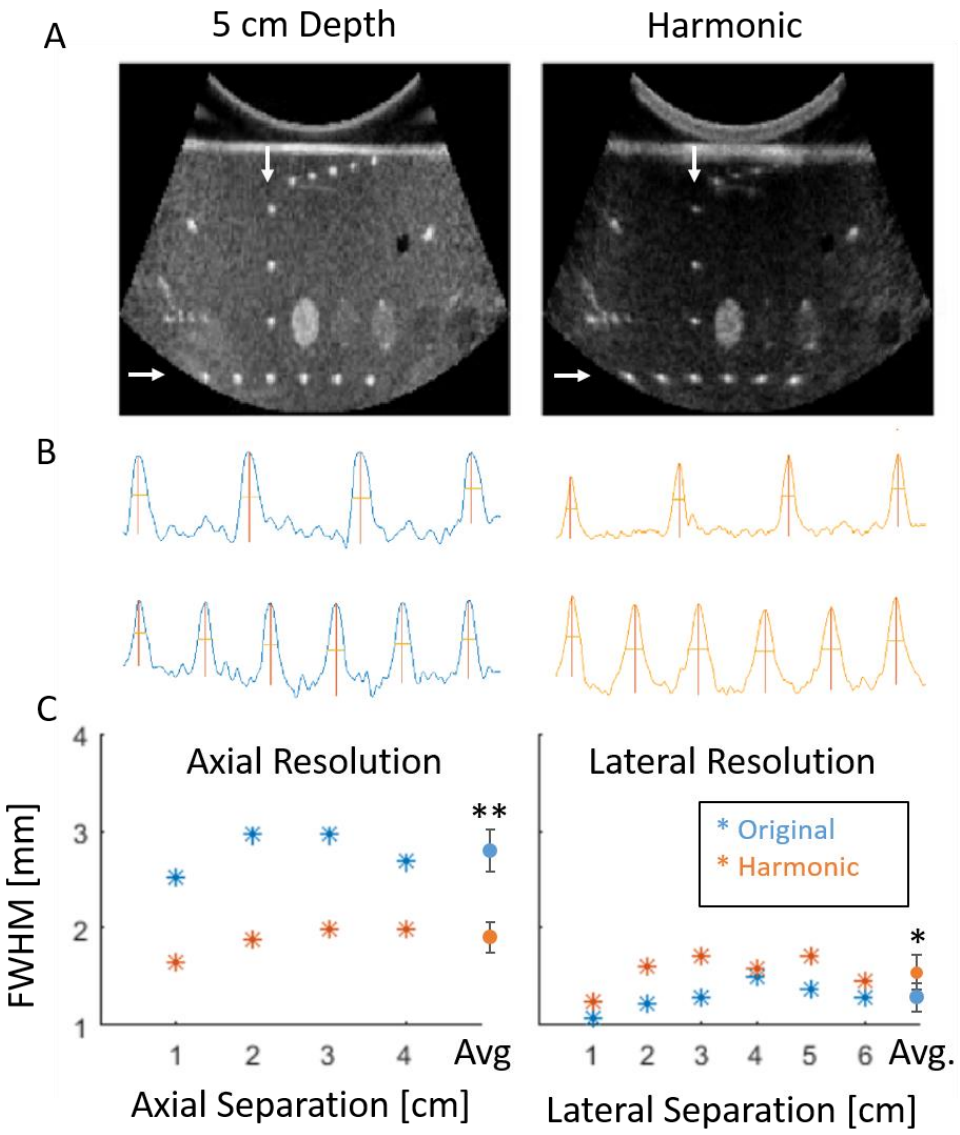

Figure 3.3 Axial and lateral FWHM analysis (5 cm). A) 5 cm depth image (left) and harmonic (right). B) Axial (top) and lateral (bottom) signals for the original (left) and harmonic (right) images. C) Full width half max plots. **P<0.001 *P<0.05

The subsequent scans, shown in Figure 3.5 and Figure 3.6, were with a maximum depth of 10 and 16 cm and utilized three focal regions (near field, mid field and far field). There was no significant difference in axial and lateral FWHM as a function of focal region. The harmonic scan yielded a significantly lower axial FWHM than the original in the mid and far region of the 10 cm depth scan. In addition, the harmonic images had a significantly lower FWHM for the wires at a depth of 4 cm and a mid-field focal region and the wires at a depth of 9 cm and the far field focal region than the original scans. The axial resolution and lateral resolution for harmonic imaging at a maximum depth of 16 cm ranged from 1.90 - 1.91 mm and 1.58 – 1.92 mm, respectively, compared to 2.13 - 2.36 mm and 1.58 – 1.82 mm for the axial and lateral resolution, respectively, for the 10 cm depth.

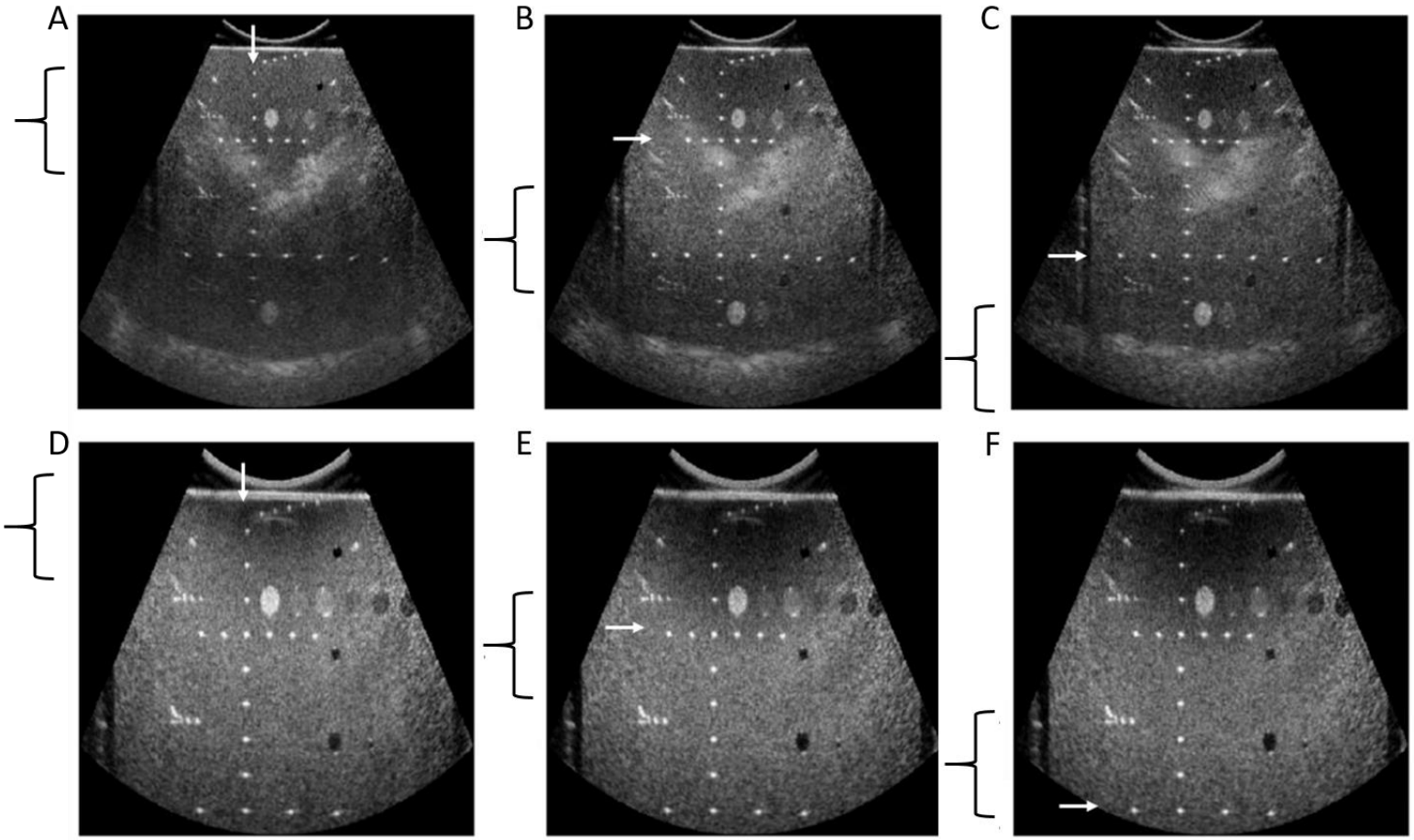

Figure 3.4 Images at 10 cm depth. A) near field, B) mid field and C) far field focal region without harmonic imaging. D) Near field, E) mid field and C) far field with harmonic imaging. Arrows point to the vertical and horizontal wire groups.

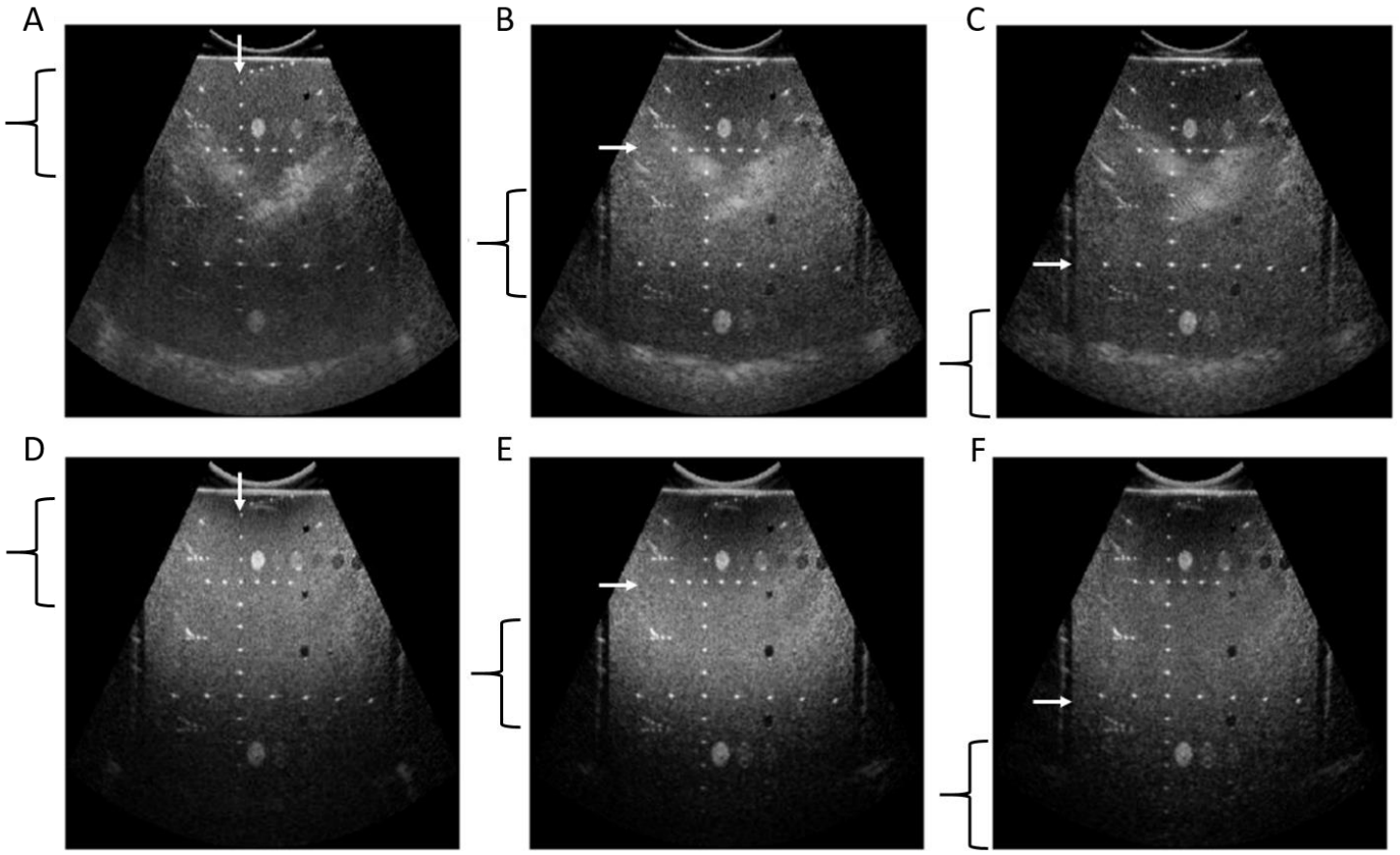

Figure 3.5 Images at 16 cm depth A) near field, B) mid field and C) far field focal region without harmonic imaging. D) Near field, E) mid field and F) far field with harmonic imaging. Arrows point to the vertical and horizontal wire groups.

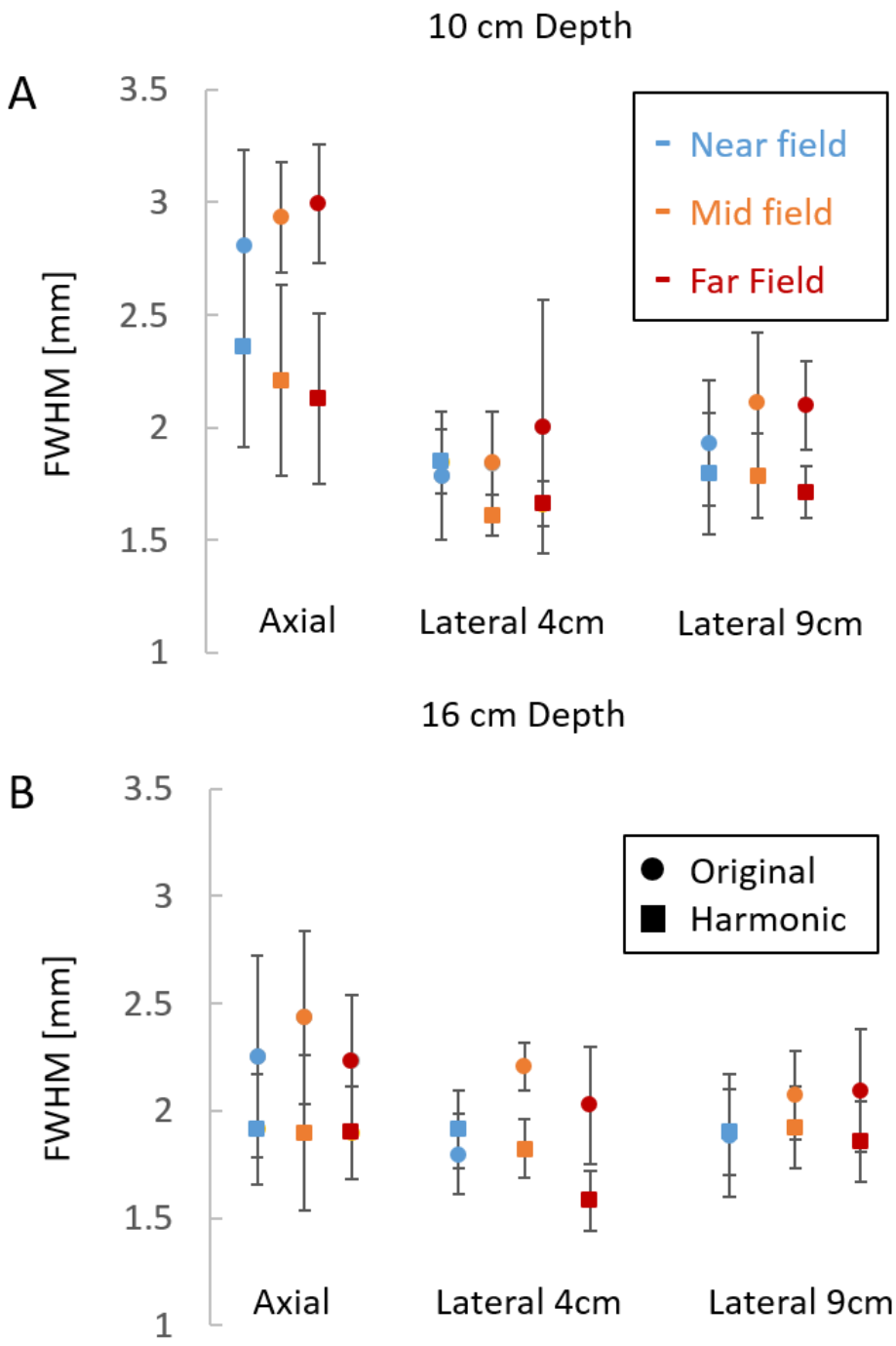

Figure 3.6 Axial and lateral FWHM analysis (10 and 16 cm). Average ± SD axial and lateral (4 and 9cm) FWHM of original and harmonic scans at three different focal regions for the maximum imaging depth of 10 cm (A) and 16 cm (B).

3.4.2 Artifacts

We retrospectively examined a series of TCC cases presented to the Purdue University Veterinary Teaching Hospital for image quality, focusing on artifacts. An example of the artifacts we identified can be seen in Figure 3.7. Rarely did comet-tail artifacts, caused by reverberation, extend into the bladder. Reverberation had the potential to blur the most anterior edge of the bladder closest to the skin and abdominal muscles, but were infrequent, small in size (1 mm) and easily identified. The combination of these features made it easy to predict where the bladder wall should be. Refractive artifacts, caused by non-perpendicular incidence of the ultrasound beam to the bladder wall, are seen as discontinuities in the bladder wall where the beam is reflected away from a particular point and there is no signal. This artifact can cause the bladder wall to "disappear," but it was typically localized and there was enough information to not interfere with accurate contouring.

Refraction, when combined with displacement artifacts caused by variations in the speed-of-sound due to tissue heterogeneities, resulted in severe discontinuities in the distal edge of the bladder wall. The largest refractive index would be caused from the beam travelling from fat (1412 m/s) to tumor (1584 m/s). By applying Snell's law, we can calculate the largest difference between the incident angle and the transmitted angle. In this case, when the incident angle is 64° the transmitted angle will be 85°. The relationship between incident and transmitted angle for this extreme case is shown in Figure 3.8A. An example of a similar case (tumor to urine) can be seen in Figure 3.8B, where the shape of the tumor causes a large incident angle, bending the beam away from the bladder wall and increasing the true path length.

Two separate path lengths are shown in Figure 3.9. If we consider a saline solution with density near that of urine, 1.05 g/L[25] and at body temperature, the speed of sound will be approximately 1554 m/s[26]. Similarly, the speed of sound in cancerous tissue is approximately 1584 m/s[27]. Therefore, the true distances to the distal edge of the bladder for the two path lengths shown cause the centroid of the bladder (and tumor) to be misrepresented, changing the absolute position of the bladder, causing the patient to be misaligned during treatment. The centroid of the bladder could move up to 2.5 mm based on contours of the bladder for different interpretations of the distal bladder edge.

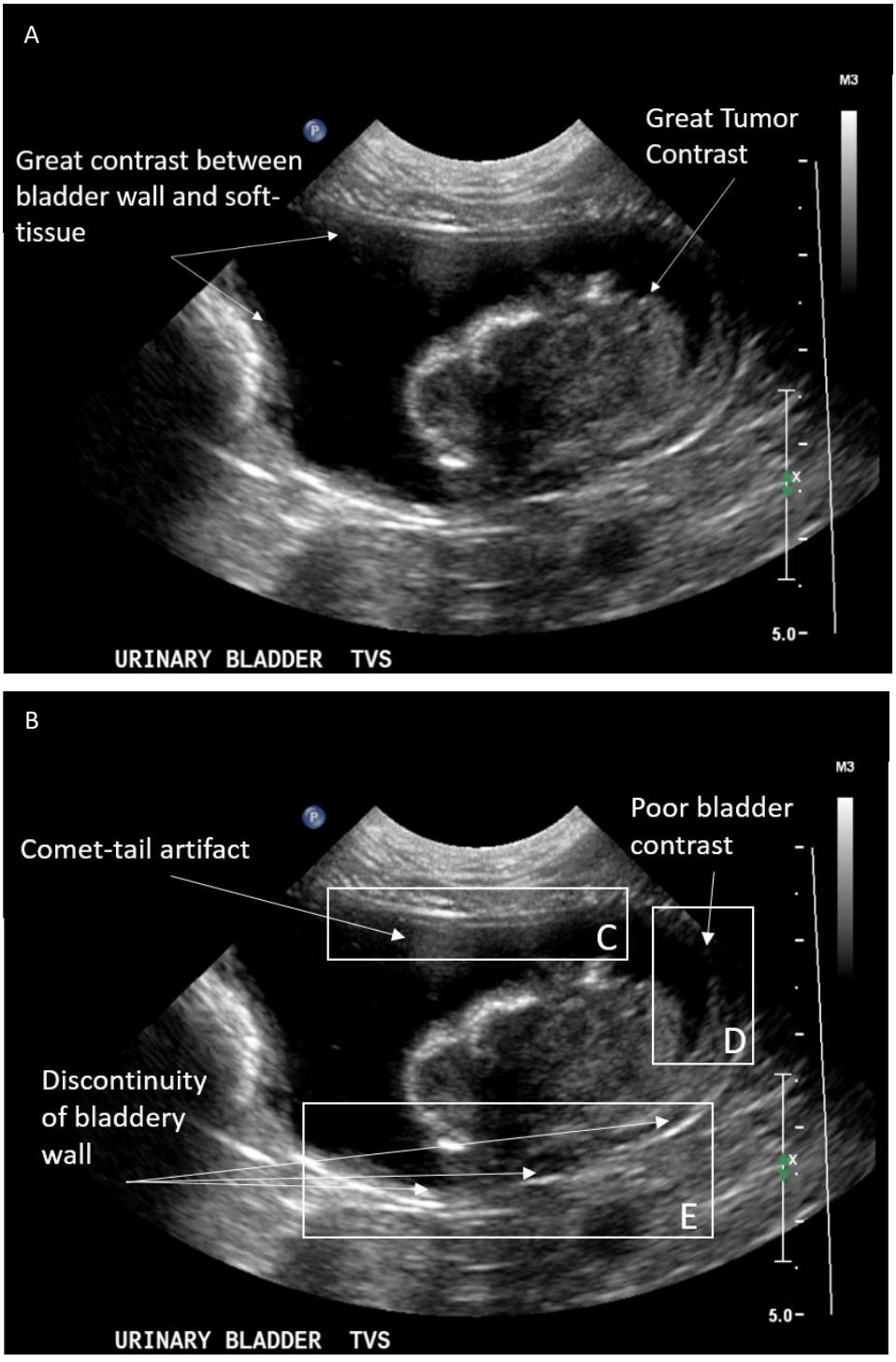

Figure 3.7 Ultrasound TCC image. A) Highlighting good bladder and tumor contrast. B) Highlighting reverberation (C), refraction (D) and speed of sound displacement (E).

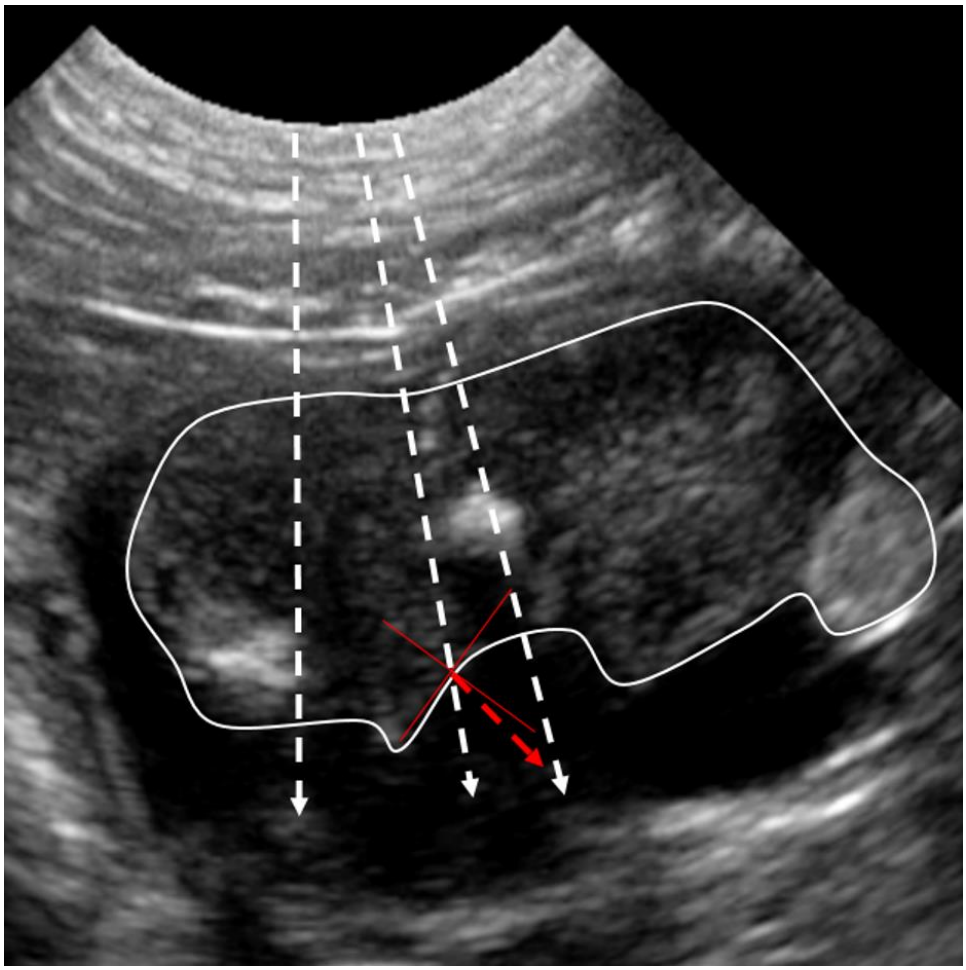

Figure 3.8 Refractive artifact**.** Extreme case of refraction (red) causing discontinuities in the distal bladder wall. Paths on the left and far right are fairly perpendicular.

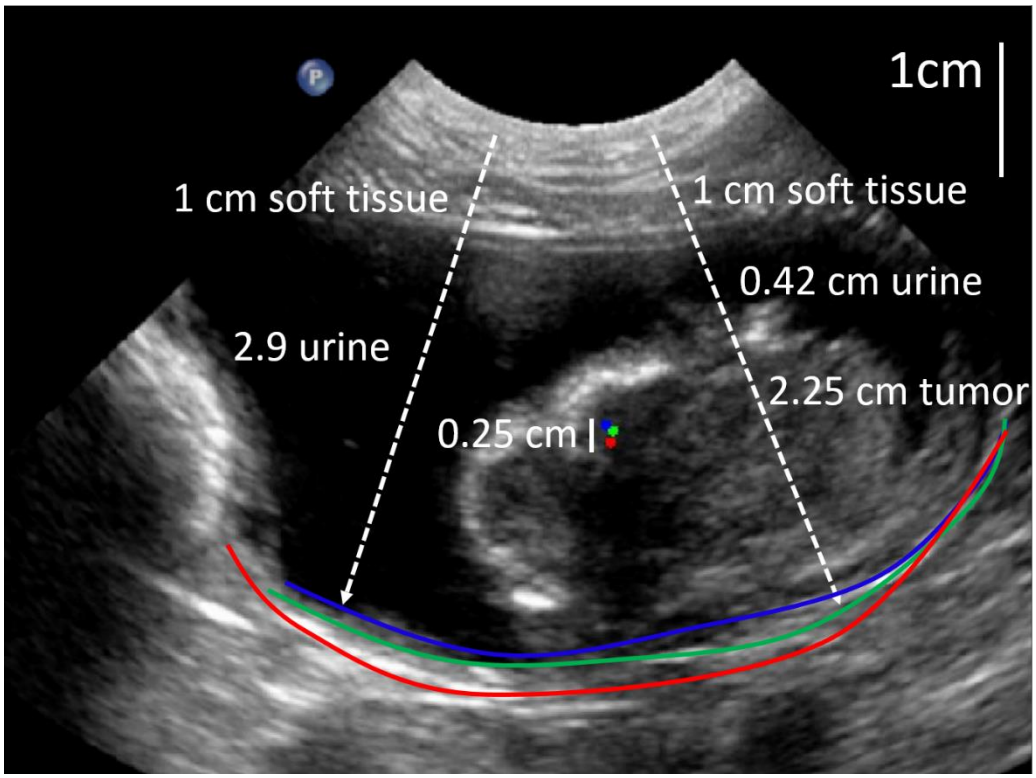

Figure 3.9 Speed of sound displacement artifact. Bladder centroid location based on three contours representing different interpretations of the distal bladder edge.

3.5 Discussion

Independent measurements of image quality of 3D-US were compared to determine an optimal set of acquisition protocols, where depth, focal region and harmonic imaging were controlled. The effects of these parameters on uniformity of spatial resolution were studied. Furthermore, a series of images were examined for the presence of artifacts that may degrade image quality. The central result from this study is that only the use of harmonic imaging had a significant effect on spatial resolution and that spatial resolution was not dependent on the FOV or the focal region. Few artifacts were present within the bladder. Of them, only discontinuities on the distal edge of the bladder were consistent. The results from Figure 3.8 demonstrate a possible 2.5 mm shift in the centroid of the bladder.

For most imaging systems, line pairs per millimeter or centimeter is a more common method for describing the limiting spatial resolution than FWHM. Line pairs per millimeter can be converted to FWHM ~ 1/(2 x LSF). Therefore, a FWHM of approximately 2mm, which closely represents our 6-2MHz broadband transducer, corresponds to 0.25 lp/mm or 2.5 lp/cm. This is considerably worse than kV-CBCT systems, but better than MV-CBCT systems, which report a range of 8-11 and 3-5 lp/cm respectively[28]. The use of MV-CBCT systems has been demonstrated, and often superior when compared to US for localization of the prostate[29,30]. These findings are counterintuitive when considering US yields comparable resolution. The comparable spatial resolutions between US and MV-CBCT and accuracy of patient alignment lead to the belief that other factors are diminishing the accuracy of US systems.

One possible explanation is the heterogeneity of the speed of sound in soft tissue. Distances in US are calculated using the time of flight of the reflected US pulse assuming a constant speed of sound of 1540 m/s in soft tissue. Recently, speed of sound correction algorithms for 3D linear[31] and curvilinear[32] probes have been published. These studies show corrections for prostate imaging can be greater than 4 mm. A second explanation could be the imaging procedure, specifically distortions caused by probe pressure. Many of the initial US based IGRT systems used free-hand imaging procedures, which could lead to inconsistent image acquisition. The only study to date, investigating the impact of probe pressure on image distortion and trying to recreate the distortions using pressure sensors yielded poorer results[33]. None of the systems appear to be trying to remove the pressure distortions through the use of a coupling medium.

3.6 Conclusions

In conclusion, the inherent resolution of 3D-US is high enough to expect alignment errors on the order of MV-CBCT. Many of the underlying physical principles of US had very little effect on the resolution of our imaging system. We observed similar resolutions whether imaging at a depth of 5, 10 or 16 cm. In addition, there was no significant change in resolution as a function of depth or whether the targets were in the focal zone in each of the subsequent scans. On the other hand, harmonic imaging showed significantly better resolution in both the axial and lateral directions when imaging at a maximum field of view depth of 10 and 16 cm. Speed of sound discontinuities of the distal bladder edge were the most visible of any of the common artifacts associated with

US imaging. The integration of already developed correction algorithms should be applied to future clinical studies.

CHAPTER 4. CONSTRUCTION OF AN ULTRASOUND GUIDANCE PLATFORM FOR IMAGE-GUIDED RADIOTHERAPY WITH THE INTENT TO TREAT TRANSITIONAL CELL CARCINOMA

4.1 Introduction

A number of US external beam radiation therapy (EBRT) guidance systems have been developed in recent years[34-36]. A detailed review of these systems both commercially available and in-house systems still under development has been published[37]. Though each system has its advantages and disadvantages, their shortcomings are: 1) transducer pressure distorts patient anatomy and since the transducer is not present during the simulation CT (artifacts), the US and CT volumes do not represent the same information and introduce significant systematic positioning errors; 2) free-hand image acquisition is highly dependent on the skill of the operator and subsequently the positional information is operator dependent; 3) free-hand probe manipulation systems can't provide intrafractional imaging because the operator would be exposed to unacceptable levels of radiation during treatment delivery.

Our objective is to demonstrate that daily 3D transabdominal US will provide accurate bladder tracking to include RT in the treatment of canine TCC. An US platform has been constructed and integrated into the treatment protocol in order to track the bladder of a canine patient while overcoming the previously

mentioned deficiencies. The objective is to determine the CT and US alignment errors within a few millimeters, which is better than or equal to CBCT. In this specific aim, the design and construction of an in-house integrated US manipulator and platform is described. To validate the US-platform, an agar-based urological tissue phantom was fabricated and used to quantify alignment errors based on rigid-body image registration in Eclipse treatment planning system. The goal is to provide a treatment procedure without the need for on-board radiographic imaging devices.

4.2 Materials and Methods

4.2.1 Construction of 3D-US platform

This platform provides a common coordinate system between CT and RT, and it serves two purposes. First, the platform provides an adaptable manipulator with reproducible positions, with error less than positional error of IMRT bed, to adapt to the patient on the CT and IMRT beds. Second, it also provides enough adaptability to align the patients so the initial conditions to the co-registration algorithm within treatment planning software converge to an optimal alignment. The US-platform defines a coordinate system based on 3D ultrasonic images that will determine the translation and rotation matrix between the CT scanner coordinate system, the 3D-US imaging system, and the IMRT coordinate system. The critical aspects of the platform are to 1) place and locate the transducer array with submillimeter precision, 2) change the angle of the transducer array to provide a means to optimize image quality, 3) assemble and disassemble quickly and easily around the patient on the CT/RT couch and 4) be

constructed out of materials that will not affect RT planning. Acrylic was used for the supports due to its low cost and speed with which it can be manufactured. The parts that could not be manufactured were 3D printed using Purdue's 3D-printing facilities. All the manufacturing was done in Purdue's Artisan and Fabrication Lab. The final design can be seen in Figure 4.1.

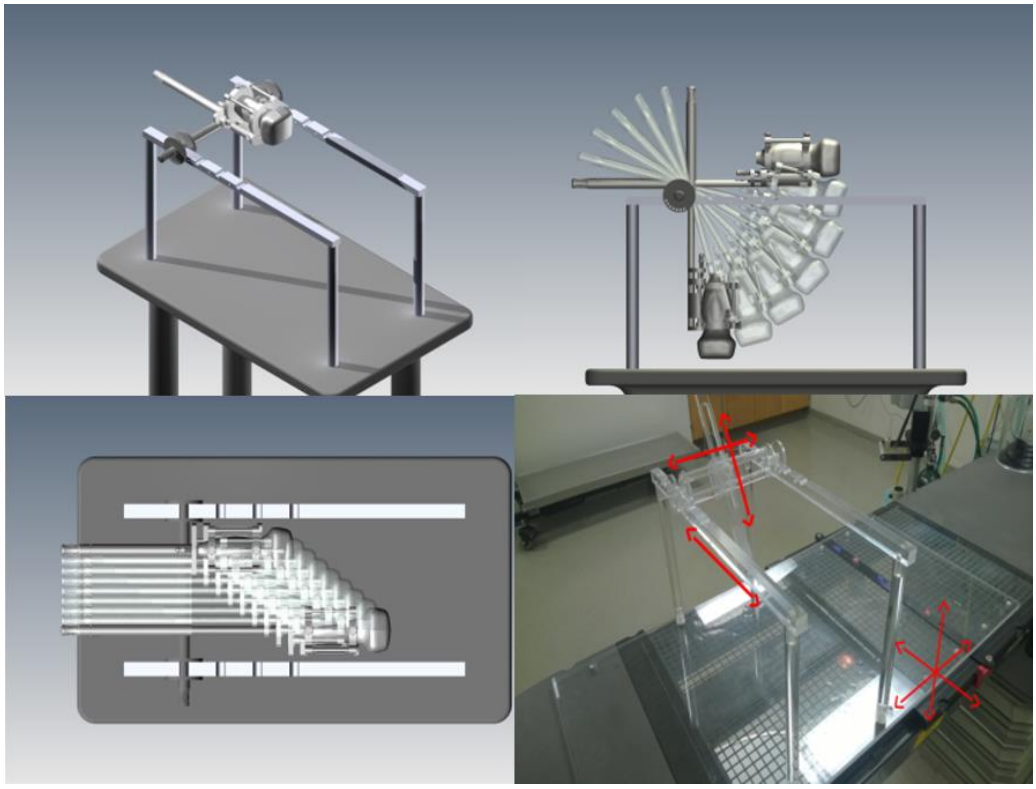

Figure 4.1 Platform design overview. A) Overview of the platform design, B) Longitudinal and lateral range, C) Different possible discrete angles of the transducer, D) different coordinate systems of the US guidance platform and the RT treatment bed.

The frame can be assembled around the patient after the patient is positioned using laser alignment. After a series of proof of concept examinations with a continuous geometry, the decision to have discrete positions would simplify setup and reduce inter-user error when trying to read angles and distances. A set of "slots" for the translating stage to rest were designed to be 5 cm apart laterally from the center, and a limited set of angles in 15° increments from which to set the transducer array position. This increased the speed with which the images could be acquired without compromising range of motion The extension of the radial arm and the longitudinal shifts are done with a 1mm threaded rod which gives us increments as fine as 10 microns.

A critical step in the US-platform design was a clamp or mold to hold and position the transducer array with high reproducibility, thus defining the central axis of the transducer array within the platform's geometry, thus relating the coordinate systems of the linear accelerator and CT bed. Three different transducer arrays were utilized throughout this study: an Acuson 8-5 2D linear array,a Philips V13-5 3D linear array, and a V6-2 3D curvilinear array. Each individual transducer array surface was modeled using a 3D infrared scanner, borrowed from the Purdue Artisan and Fabrication Lab. The transducers were positioned on a black surface with the directional marker on the side. This was because the transducers are mirrored about that plane. Therefore, we only needed to scan half of the transducer and the other half was modeled in Catia™ (Dassault Systémes, Walthman, MA, US). Reflective stickers provided by the 3D scanner were placed on and around each of the transducer arrays, scans were acquired, and files were exported in the STereoLithography (stl) format and imported into the Catia™ environment for rendering. Once the designs were completed, the model for each

transducer array was 3D printed using a filament based thermoplastic (PLA, $\rho = 1.25$ g/cm^3) to be used as a CT safe placeholder transducer. With these same surface renderings, clamps were designed to form-fit each transducer. Individual clamps are interchangeable with the platform.

We calibrated the US-platform to the coordinate system of the linear accelerator by first selecting an "origin", where one of the discrete positions on the platform was chosen and the x, y, and z coordinates of the treatment couch recorded. To determine the precision, we defined discrete positions of the TA within the platform, used the geometry to predict the new coordinates of the couch and then moved the couch to determine the error using an in-house MATLAB™ (The MathWorks, Inc., Natick, MA) graphical user interface (GUI).

4.2.2 Developing a Urological Phantom of the Bladder

To incorporate the US-platform into the treatment planning protocol, a soft tissue phantom was fabricated with the acoustic and CT properties consistent for a patient with bladder cancer, in this case a dog with TCC. The phantom was constructed based on the anatomy obtained from CT and US scans of a dog, tissue types and geometric dimensions (see Figure 3.7 and 3.8). This phantom was molded in a 12 x 12 x 12 cm acrylic container, with a 3 mm layer of skin, 1 cm layer of fat, 1 cm layer of muscle, and 25 mL ellipsoid (balloon) of 5% NaI saline (urine), embedded within a 7 cm layer of soft tissue. The CT and 3D US images of the bladder phantom are displayed in Figure 4.2. The phantom is a mixture of agar, glycerin and physiological saline, where the proportion of

each element is chosen to control the density and speed-of-sound consistent with skin, muscle, soft tissue and bladder.

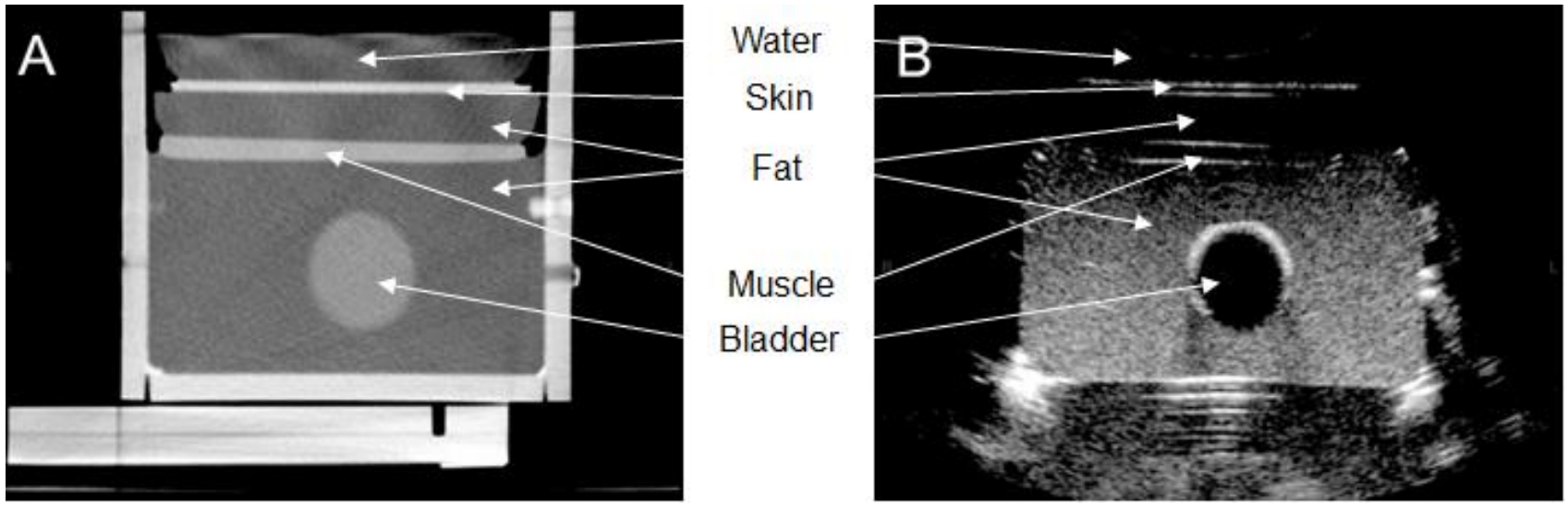

Figure 4.2 Phantom. A) CT slice of phantom, B) corresponding US slice

The solutions were brought to a boil in a microwave and then stirred constantly while they came down in temperature. When the solution reached 40^{o}C they were transferred to the phantom. At this temperature the solution would turn to gel quickly when left undisturbed. This consistently produced mediums with the most uniform set of acoustic and CT properties and minimal air bubbles. The balloon was suspended within the plexiglass container of the phantom by running a suture through the balloon, just above the knot. The soft tissue agar solution was poured to cover the balloon. When the solution was set, the suture was pulled through and removed. Saran wrap was used between mediums to keep the glycerin from leeching out. A flat edged block was used to push any air bubbles that formed between the wrap and the agar to the edges. A final layer of saran wrap was placed on top as a seal. By evaluating the CT and US images, we found that the physical properties of the phantom remained consistent for about 3 weeks when stored at room temperature.

To determine the density and speed-of-sound of the different tissue types of the phantom, CT and photoacoustic was used. For the former, the average value of Hounsfield units for each tissue type using CT was calculated, and then converted to density based on the calibration curve obtained from a QA CT phantom (Gammex 464 ACR CT Phantom). To determine the speed of sound, photoacoustics methods were employed. A point source, fishing line with one end dipped in india ink, was placed at the bottom of beaker. This absorber was exposed to a laser source and the resultant photoacoustic signal was measured using an ultrasound transducer at two distances 1 cm apart. The time at which the peak signal was measured at both transducer locations was used to calculate the speed-of-sound for each tissue type. To validate this technique, the

speed-of-sound for distilled water at temperatures ranging from 4°C to 50°C was measured and compared to the literature (Figure 4.3). This same method was used to determine the speed of sound of different concentrations of distilled-H_2O (dH_20) and glycerin, assuming the speed of sound for a mixture of dH_2O and glycerin followed a linear model. For example, water at 25°C has a speed of sound of 1494m/s and pure glycerin travels at 1920m/s. Thus,

$$C_{50/50} = 0.5 * 1920\left[\frac{m}{s}\right] + 0.5 * 1494\left[\frac{m}{s}\right] = 1707\left[\frac{m}{s}\right] \quad (4.1)$$

We measured distilled water and 2% agar to determine if the agar was affecting the speed of sound.

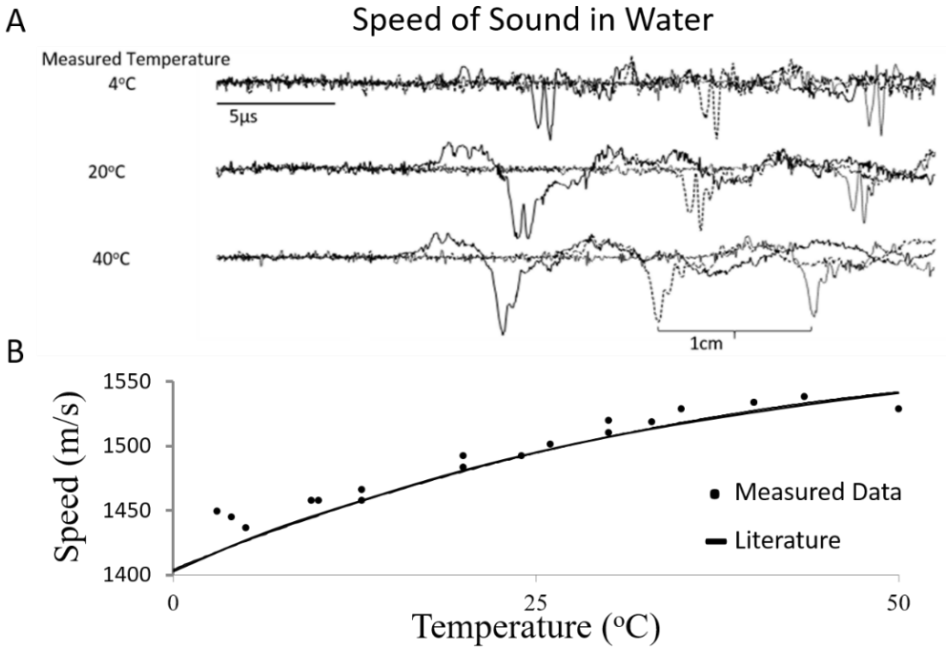

Figure 4.3 Photoacoustic validation of the speed of sound in water. A) Sample photoacoustic signals showing the speed of sound differences as a function of temperature. B) Measured data and function fit to the literature values.

4.2.3 Imaging Protocols

B-mode ultrasonography of all phantoms was performed with a dedicated ultrasonography machine (Philips iU22 SonoCT system, Philips Ultrasound, Bothell, WA). A broadband volume curved array transducer (6-2 MHz) and/or a broadband volume linear array transducer (13-5 MHz) were utilized. The depth, focal spot and window level were adjusted to optimize image quality, resulting in a 512 x 510 matrix with a 0.42 x 0.30 x 0.6 mm voxel size (see Specific Aim 1). The probes were positioned in a transverse plane for all imaging studies. All phantoms were scanned using a 64-slice helical CT scanner (GE Lightspeed 64 Slice CT Milwaukee, WI, USA) using the following parameters: kVp of 120, mA of 300-500, slice thickness of 2.5 mm, pitch of 1.0, variable scan field of view, 512 x 512 matrix, rotation time of 1 s. Resulting in a 0.54 x 0.54 x 2.5 mm voxel size.

4.2.4 Image Registration

The volumes need to be co-registered with the CT scans used in the IMRT treatment planning software in order to be used as a method for patient positioning. We wanted to do all the registrations in Eclipse Treatment Planning system. In order for Eclipse to recognize the US images, a MATLAB^{TM} script was developed to create dicom files for the 3D-US volumes, which were exported from the US unit's hard drive to a removable media device and then loaded into MATLAB^{TM} through a dedicated folder. We separated the metadata (dicom headers) from a CT slice, stripped the header information and saved the file as a CT template. The template with dicom data pulled from the US volumes. Unlike CT where each slice stands on its own, the US volumes are

exported from the unit as one 3D matrix. We used a script to separate each slice from the exported volume, assign new metadata with the correct positional (couch and platform coordinates) and voxel information and write new dicom images. The files could then be imported into Eclipse using the dicom media file import filter as if they were CT scans.

When a patient, canine, human, or urological phantom, is moved from the CT scanner to the RT suite, the patient and 3D-US platform is repositioned on the treatment couch at nearly the same position through the use of PinnPoint Lok-Bar™ (CIVCO Medical Solutions, France) and laser alignment. An US volumetric image is acquired and processed using the previously mentioned methods, and co-registered to the treatment planning CT images within Eclipse. The transformation matrix is used to modify the RT treatment bed to match CT and RT coordinate systems. Critical to this protocol is the ability to accurately and precisely co-register either the treatment US volume to the simulation US/CT volume. To measure these parameters, the bladder phantom was translated and rotated relative to the US transducer array. The experimental setup for these tests is shown in Figure 4. For each measurement, the phantom was rotated (using a rotating platform) over a 0-45 degree range -- at angles rotated 5, 15, 30 and 45^{o} around the vertical axis -- and the transducer was translated over a 0-20 mm range in different increments, after which a CT and US scan was acquired. This procedure was repeated after inserting a 4° wedge to change the patient pitch.

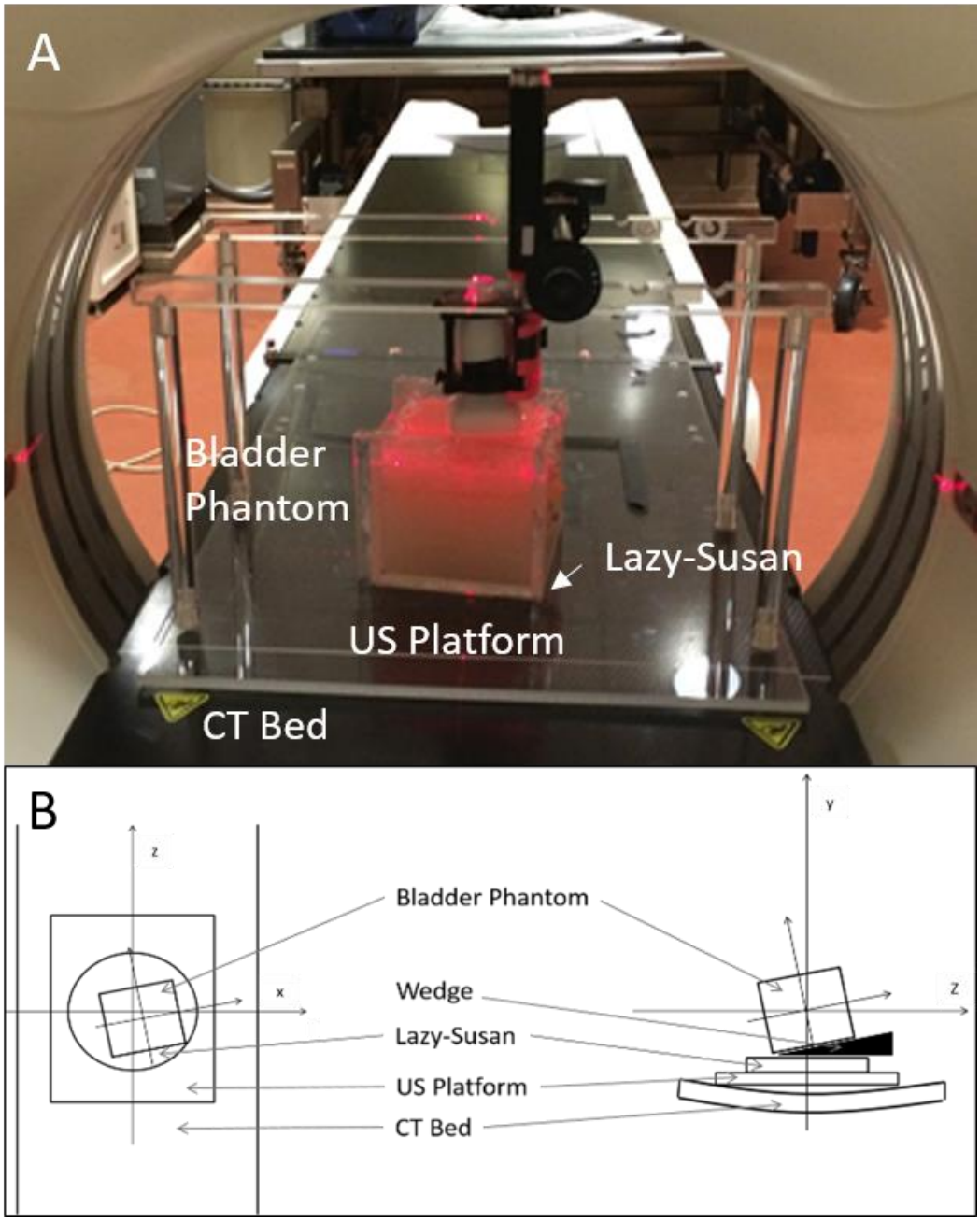

Figure 4.4 Experimental design. A) Picture of the phantom and platform in the CT scanner with the placeholder transducer in place. B) Components involved in the experimental design

Each subsequent scan was co-registered to the scan taken with the phantom in the flat position (and a wedge angle of zero). The registration matrices composing of the x, y and z translation and α, β, and γ rotational components (Euler angles) were recorded. For the US scans, the transducer array was held in a clamp above the phantom and the experiment was repeated three times for each set of rotation angles (N=3). The US and CT volumes were co-registered using the software in Eclipse, which will be compared to the CT-CT co-registration. For each registration, the first modality is the source volume and the second is the target volume.

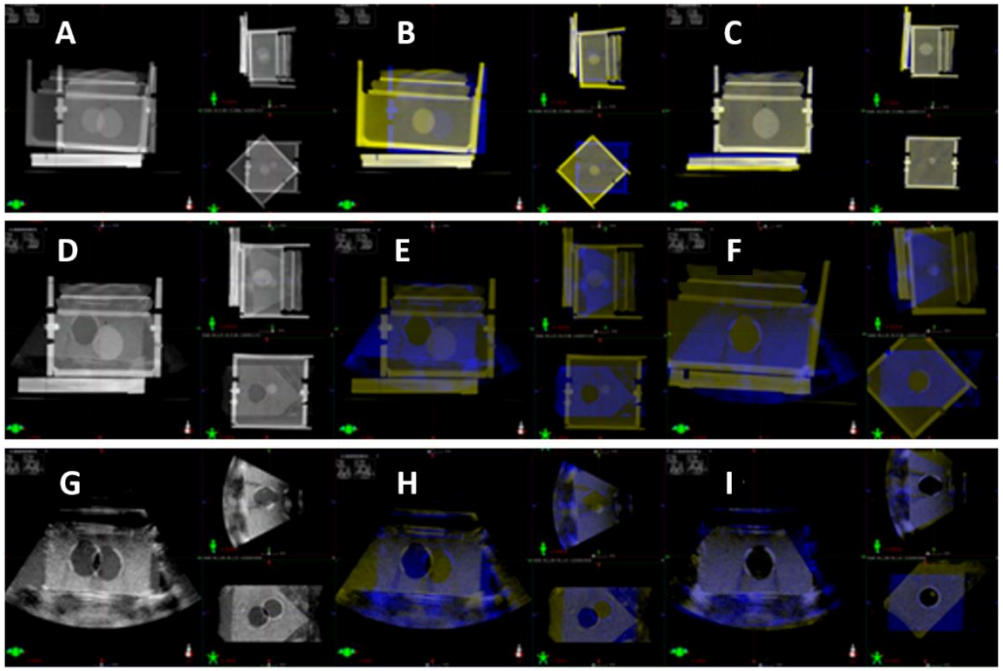

Figure 4.5 Volume Registrations. A-C) US-CT registration for phantom in the 'flat' position. The pre-registered volumes can be seen in (A), the same window in color in (B) and the registered volumes in (C). Transformation matrices for each rotation can be found in Table 3. D-F) CT-CT registration between the phantom rotated to 45º and the flat position. G-I) US-CT registration between the phantom rotated to 45º and the flat position. J-L) US-US registration between the phantom rotated to 45º and the flat position. The transformation matrices for D-F, G-I and J-L can be found in Table 4.4.

Our standard method for co-registration included, first assuming no a priori knowledge. We made no manual movements or changes to the image before attempting an automatic registration. The details powering the Eclipse™ automatic registration are proprietary, but the underlying merit function is based on mutual information. If by visual inspection the automatic registration failed, then a rough manual match was applied. If the automatic registration still failed, then the field of view was modified to include only the "tissue," then only the skin, muscle and bladder and lastly, only the bladder. Lastly, image intensity thresholds were adjusted if all else failed. All US-to-US and CT-to-CT registrations could be successfully automatically registered whereas the US-to-CT registrations were done manually.

4.3 Results

4.3.1 Construction of 3D-US platform

The purpose of the US-platform was to reduce uncertainty in patient positioning prior to IMRT. Therefore, the ability of our platform to be calibrated to the coordinate system of the linear accelerator was critical in our final evaluation. During initial testing, a systematic error stemming from the platform not being square to the treatment room lasers was identified. Over the lateral range of the RT couch, the longitudinal and vertical offsets were 2mm and 1mm respectively. These offsets were viewed using the room lasers and in the image registration. To evaluate patient realignment uncertainty, the arm of the platform that holds the transducer array (TA) was positioned at the treatment room iso-center and then the TA was rotated through each discrete angle at which the central

ray normal to the TA surface. This process was repeated and the average and standard error calculated. The errors between what we calculated based on the geometry of the platform and the true couch readings are shown in Table 4.1 with a diagram of the experiment in Figure 4.2

The platform design provides a reproducible coordinate system for US volumes to be registered to CT for patient positioning in the RT suite. The acrylic supports caused light streaking artifacts and could be avoided completely by selecting a field-of-view that avoids the supports. Although PLA has a higher density than acrylic, the use of a honeycomb infill pattern reduces the overall density of the printed parts and further reduced streaking artifacts. We attempted a handful of prints using the thermoplastic Acrylonitrile Butadiene Styrene (ABS) because of its lower density and effective Z than PLA, but we found ABS to be much more difficult to work with and produce parts of good enough quality to be used. Further studies developing optimal printer settings would be beneficial to groups looking to use 3D printed parts in radiology and RT.

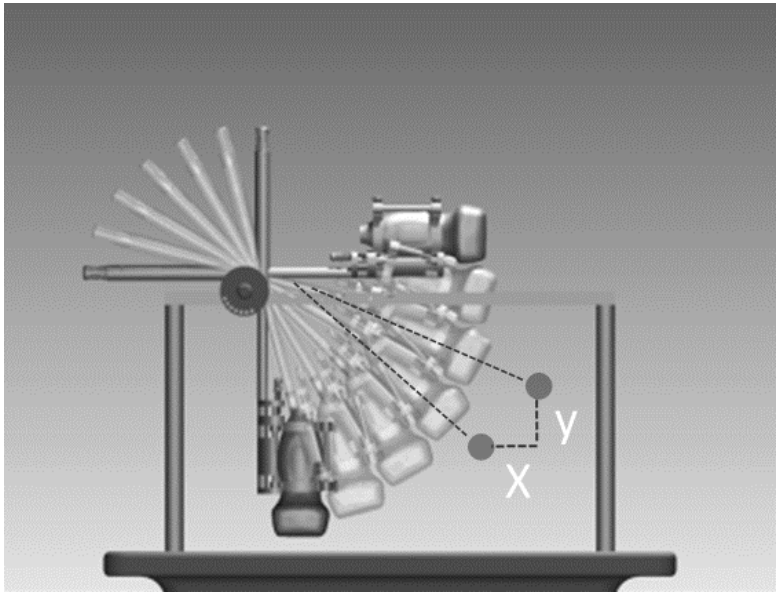

Figure 4.6 X shows the lateral shift, Y shows the vertical shift and the longitudinal shift is in and out of the page.

Table 4.1 Errors between predicted couch position and actual couch position [mm] for moving the transducer from 75° to 60°, 60° to 45°, etc.

	75 → 60	**60 → 45**	**45→30**	**30 → 15**	**Average**
vrt	-0.22 ± 0.9	0.13 ± 0.89	-0.16 ± 1.28	0.25 ± 1.11	**-0.00 ± 0.99**
lng	-0.20 ± 0.84	-0.20 ± 0.84	0.60 ± 0.55	0.20 ± 0.45	**0.10 ± 0.72**
lat	0.46 ± 1.29	0.03 ± 0.81	0.18 ± 0.83	0.06 ± 0.55	**0.18 ± 0.85**

4.3.2 Developing urological phantom of the bladder

Results for the density and speed-of-sound measurements are shown in Figure 4.7. In Table 4.2, the recipe for constructing agar-based tissue phantoms with the necessary density and speed-of-sound consistent with skin, muscle, fat and the bladder and their corresponding values as measured by CT and US is displayed. Tissue phantom density was measured using CT, where the relationship between density and Hounsfield units was measured using the Gammex 464 CT Phantom and the calibration equation (Figure 4.7(A))

$$y = .001x + .9939. \tag{4.2}$$

The linear model assumed in equation 5.1 fit the data with an $R^2 = 0.972$ for the speed of sound with a range of concentrations of glycerin. Agar increased the speed of sound compared to dH2O from 1497 to 1506 m/s at 25°C. The speed of sound for cooked agar and dH2O can be seen in Figure 4.7(C).

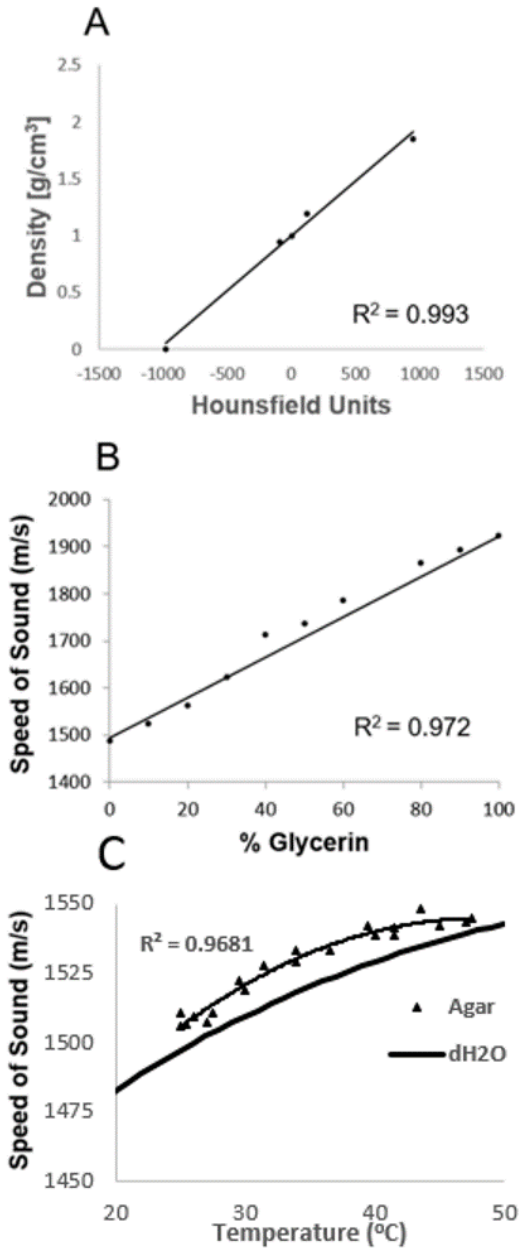

Figure 4.7 Phantom density and speed of sound validation. A) CT QA phantom calibration. From left to right: air, polyethylene, water, acrylic, bone. B) Measured speed of sound as a function of glycerin concentration compared to predicted values from equation 1. C) Measured speed of sound of 2% agar as a function of temperature. Solid line indicates the accepted speed of sound of water.

Table 4.2 Recipe for phantom with measured CT number [HU], density [g/cm^3] and speed of sound [m/s] with corresponding values found in the literature

	Recipe		Measured			Literature	
	% Glycerine	% Agar	CT Number	Density**	Speed of Sound	Density	Speed of Sound
Water	0	0	-1.21 ± 2.64	0.993	1493	0.998[38]	1483[39]
Skin	50	2	107.34 ± 3.49	1.098	1703*	1.110 - 1.119[25]	1590-2170[40]
Fat	0	2	2.66 ± 2.67	0.996	1487*	0.916[25]	1412 - 1487[41]
Muscle	25	2	69.65 ± 3.91	1.061	1595*	1.038-1.056[25]	1589 - 1603[41]
Urine	0	0	41.51 ± 0.87	1.034	--	1.001-1.050[25]	1554[26]

Phantom measured at room temperature. *Calculated from equation (4.1). **Calculated from equation (4.2). Literature speed of sound measurements mostly from canine tissue. Literature density values from human tissue.

4.3.3 Image Registration

First, we examined the ability of our processing methods to successfully import US volumes into Eclipse™ (Varian Medican Systems INC., Palo Alto, CA.). The US volumes could not be imported into Eclipse when sent through PACS, either via the import wizard or the DICOM import/export window. This was due to the DICOM headers for CT and US data being different. To resolve this mismatch in format, a CT file was used as a template, where the header parameters SliceThickness, PixelSpacing, InstanceNumber, ImagePatientPosition and PatientPosition were redefined based on US imaging protocols. Caution needs to be taken when setting the x, y and z resolution as they were very dependent on the settings of the US unit at the time of the volume acquisition. For example, the field-of-view had a direct effect on the voxel sizes. Validation of the voxel size assignment is shown in Figure 4.8. The lateral phantom width was measured in CT (12.03 cm) and US (12.35 cm) for an error of 3.2 mm. Additionally, we measured the distance from the surface of the skin layer to the bottom of the phantom in both CT (8.89 cm) and US (9.05 cm) for an error of 1.6 mm. Although, the z-position, or slice location, could easily be defined with a simple calibration, the x and y positions are dependent on where the target is in the image in relation to CT and thus needed to be registered to the CT to be known. However, this information was not necessary to successfully determine the transformation matrices between the subsequent US volumes.

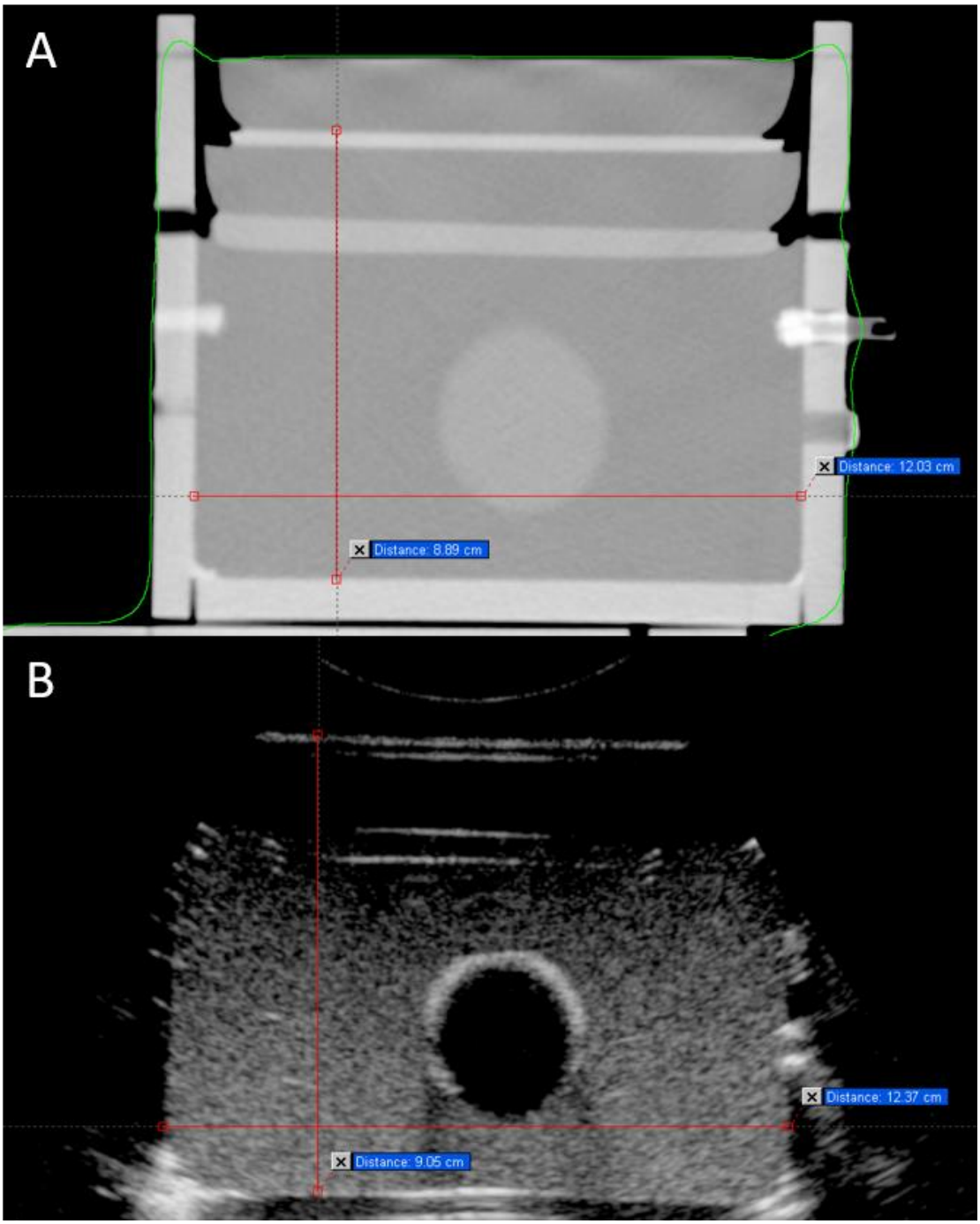

Figure 4.8 Voxel size assignment. A) CT of phantom with the lateral (12.03 cm) and vertical (8.89 cm) measurements shown. B) US of phantom with the lateral (12.37 cm) and vertical (9.05 cm) measurements shown.

The accuracy and precision of US-US and US-CT registrations will determine patient alignment/realignment but also the appropriate treatment margins within and between fractions, respectively. The accuracy in phantom positioning (and thus realignment) was determined by calculating the average difference in the translational and rotational components of the transformation matrix between two registered volumes, and the precision of these measurements by their standard deviation. Each US volume was registered to its CT counter-point to determine the initial offsets between the US and CT coordinate systems. Those measurements are shown in table 4.3. The average translational offsets were -59.53±0.35 mm, -87.26±0.28 mm and 78.27±1.12 mm in the X, Y and Z components, respectively; and their average rotational components were -1.47 ± 0.35°, 1.77 ± 0.88° and -0.08 ± 0.34° in the X, Y and Z. The small standard deviations suggest high precision when registering US to CT.

Table 4.3 US-CT translational [mm] and rotational [degrees] components of the transformation matrices

		Flat	Wedge	5	15	30	45	**Average**
Translational	X	-59.23 ± 0.74	-59.93 ± 0.29	-59.73 ±1.20	-59.20 ± 0.26	-59.87 ± 0.21	-59.23 ± 0.38	**-59.53 ± 0.62**
	Y	-87.17 ± 0.47	-87.40 ± 0.78	-87.43 ± 0.57	-86.73 ± 0.67	-87.50 ± 0.44	-87.33 ± 0.12	**-87.26 ± 0.53**
	Z	80.17 ± 1.23	78.23 ± 0.93	77.8 ± 0.00	78.73 ± 0.68	77.83 ± 0.45	76.83 ± 0.74	**78.27 ± 1.24**
Rotational	X	-1.63 ± 0.40	-1.43 ± 0.76	-0.80 ± 0.75	-1.83 ± 0.83	-1.50 ± 0.70	-1.60 ± 0.10	**-1.47 ± 0.64**
	Y	0.50 ± 0.87	1.50 ± 0.10	-1.57 ± 0.40	1.53 ± 1.34	2.53 ± 0.67	3.00 ± 0.40	**1.77 ± 1.04**
	Z	-0.13 ± 0.23	-0.50 ± 0.87	-0.30 ± 0.26	0.50 ± 0.78	0.00 ± 0.20	-0.07 ± 0.06	**-0.08 ± 0.53**

We used the CT-to-CT registrations as the gold standard and US-to-US and US-to-CT registrations to determine the precision in realignment. Each US volume was registered to the phantom in the Flat position for US and CT. The US-to-CT transformation matrices were subtracted from the average US-to-CT transformation matrix from Table 4.3 to correct for different initial coordinate systems. The average translational components and standard deviations of those transformation matrices are shown in Table 4.4.

Table 4.4 Translational [mm] and rotational [degrees] components of transformation matrices. The wedge creates a 4° rotation about the x-axis. All other rotations are about the y-axis

Translational

		Wedge→Flat	5→Flat	15→Flat	30→Flat	45→Flat
	CT	-0.6	1.3	3.6	2.5	-3
X	US-US	0.31 ± 0.18	8.03 ± 0.55	22.10 ± 0.20	34.30 ± 0.20	35.00 ± 0.95
	US-CT	-0.93 ± 1.11	1.17 ± 0.66	7.80 ± 0.52	20.23 ± 0.78	36.86 ± 0.46
	CT	4.7	4.3	3.3	1.8	0.4
Y	US-US	9.46 ± -0.07	8.93 ± 0.06	8.27 ± 0.06	6.70 ± 0.20	4.43 ± 0.57
	US-CT	4.63 ± 0.67	3.77 ± 0.72	5.03 ± 0.23	4.8 ± 0.44	5.27 ± 1.18
	CT	-4.7	1.4	14.8	35.6	55.1
Z	US-US	2.90 ± 0.26	13.03 ± 0.91	39.70 ± 0.46	83.97 ± 0.83	126.20 ± 1.66
	US-CT	-4.10 ± 0.38	0.40 ± 1.04	13.13 ± 1.04	27.5 ± 0.57	39.03 ± 1.15

Rotational

		Wedge→Flat	5→Flat	15→Flat	30→Flat	45→Flat
	CT	3.6	3.7	4	4.4	6
X	US-US	4.01 ± 0.01	3.93 ± 0.06	4.30 ± 0.00	4.83 ± 0.12	5.77 ± 0.72
	US-CT	2.87 ± 0.90	4.37 ± 0.85	4.20 ± 1.01	5.03 ± 0.51	1.9 ± 2.52
	CT	0.4	-4.3	-14.4	-29.6	-44.3
Y	US-US	-0.04 ± 0.06	-4.53 ± 0.31	-14.70 ± 0.17	-30.37 ± 0.31	-44.50 ± 1.05
	US-CT	0.70 ± 1.23	-3.80 ± 1.21	-14.30 ± 0.85	-28.03 ± 0.81	-42.57 ± 0.75
	CT	-0.1	-0.6	-1.3	-3.1	-4.5
Z	US-US	-0.16 ± 0.06	-0.40 ± 0.00	-0.83 ± 0.06	-1.57 ± 0.15	-2.97 ± 0.72
	US-CT	-0.3 ± 0.44	-0.43 ± 0.06	0.80 ± 0.10	0.30 ± 0.56	0.33 ± 1.92

The variation in the translational offsets between CT, US-US, and CT-US can be explained by the different point at which each volume was rotated around. The phantom physically rotates around the center of the lazy susan, the CT volumes rotate around the iso-center and the US volumes rotate around the corner of the volume. Identifying a method to match the volume origins to remove this systematic error was unsuccessful. For example, the DICOM origins could be matched in the contouring window of Eclipse™, but didn't carry over to the Registration window. We also attempted to pad the volumes in MATLAB™, but a standard protocol could not be found to work for every volume and processing each volume became too time consuming to be considered practical in a clinical environment. Therefore, the procedure was abandoned. The rotational components were not affected.

The statistical error, or precision, is determined from the standard deviations within each group of registrations. Large statistical errors can't be corrected for and call for large target margins. For US-US registrations, the statistical errors were small, with an average of 0.42, 0.19, 0.82 millimeters for the x, y and z translational components, respectively, and an average of 0.18, 0.38 and 0.20° or the x, y and z rotational components, respectively. Statistical errors from US-CT registrations were larger, an average of 0.71, 0.65 and 0.84 mm for the x, y and z translational components, respectively, and an average of 1.16, 0.97 and 0.62 degrees for the x, y and z rotational components, respectively.

4.4 Discussion

We have proposed to develop the tools necessary for clinics to implement ultrasound guided RT using systems already available to most hospitals and fabricated with inexpensive and low-Z materials. The US-platform was built out of acrylic and PLA and provided a reproducible frame of reference for 3-D ultrasound volumes to be registered to CT treatment planning scans. The platform doesn't produce CT artifacts and can be assembled quickly and easily while the patient is on the CT/RT couch. To test the applicability of the US-platform, a rigid phantom comprised of agar, glycerin and water was developed to represent the abdominal features seen in both CT and US. Under different rotational and translation conditions found in the clinical, the US volumes were imported into Eclipse and registered to CT after being processed in MATLAB™. The resulting registration matrix elements were used to shift the couch to align the patient (or phantom) to the treatment planning CT. Validating this technique when aligning canine patients needs further investigation.

The patient is imaged via US and CT on the simulation bed to ensure the images represent the same anatomy. The CT is used for treatment planning within Eclipse. US volumes are taken with the patient on both the IMRT treatment couch and the CT bed, and then registered to either the initial CT or US to determine couch shifts that will realign the treatment images with the simulation images. We discovered that the process of importing the US volumes to the treatment planning system was nontrivial, requiring reformatting of the US volumes. When using the US-platform, there were a number of uncertainties. One, the mechanical movement of the platform was within the 2 mm acceptable tolerance defined by quality assurance procedures[42] and detectable limits due

to the precision of the couch. The phantom movement registrations were consistent with previously reported accuracies[43-45]. The multimodal registration accuracy was much worse due to the software not being able to register the volumes automatically. The inability to automatically register US to CT presents an opportunity to improve the precision of US greatly as a positioning tool.

Table 4.5 Ultrasound platform measurements compared to quality assurance guidelines from TG report 142

Positioning/repositioning	
Planar kV and MV imaging	≤2 mm
kV and MV CBCT	≤2 mm
Ultrasound	0.21 ± 1.49 mm
Coordinate Coincidence	
Planar kV and MV imaging	≤2 mm
kV and MV CBCT	≤2 mm
Ultrasound	1.99 ± 1.42 mm*

Ultrasound maximum 5° Rotation. Distance calculated from US-to-CT values in Table 4.4

While acrylic was adequate for building a prototype platform, it was too brittle to effective as a long term tool without extreme caution taken to prevent wear and tear. The 3D printed materials would be more efficient, but the quality of the prints needs to be improved or the design altered as the ability to print functioning parts has not been perfected. We believe carbon fiber would be the ideal material.

Agar-based phantoms are inexpensive to make and with the addition of glycerin to mimic different soft tissues; other centers should be able to duplicate the results presented and explore different uses not considered by the authors. The authors believe these US-platform designs promote further manufacturing and 3D printing studies for tissue- and air-equivalent materials typically used in RT, such as carbon fiber. The methods for importing ultrasound volumes into treatment planning systems will allow for new multi-modal image fusion and registration studies to be investigated, such as power Doppler.

4.5 Conclusion

The purpose of this work was to develop an ultrasound guidance system solely on equipment available to nearly all institutions. Based on our results, patient setup uncertainty is consistent with currently used techniques for positioning prostate patients if couch-repositioning is less than a 5° rotation. Further investigation into the different origins between US and CT may expand the conditions for which the registration matrices accurately depict the couch shifts. Additionally, incorporating methods to automatically register US to CT, such as point matching, will improve the precision of the whole system. This work builds on the literature promoting ultrasound to be a viable

option for image-guided RT, specifically for clinics not willing or not able to buy commercially available equipment. Additional design considerations include the future use of ultrasound-based functionality (photoacoustics, radioacoustics, Doppler) to monitor blood flow[46] and hypoxia[47] and/or in-vivo dosimetry for applications in other therapeutic techniques, such as hyperthermia, anti-angiogenesis and particle therapy[48].

CHAPTER 5. VALIDATING HEMOGLOBIN SATURATION AND DISSOLVED OXYGEN IN TUMORS USING PHOTOACOUSTIC SPECTROSCOPIC IMAGING

5.1 Introduction

Photoacoustic tomography (PAT) is a noninvasive and nonionizing imaging modality utilizing laser-induced ultrasonic signals. This imaging method merges the high resolution of ultrasonic signals with the contrast being provided by optical scattering and absorption. This allows for non-invasive structural and functional imaging in-vivo[12]. Pulsed laser energy is absorbed instantaneously into the tissue, causing the tissue to expand due to heating. The expanding tissues push against the surrounding tissue forming an acoustic (or ultrasonic) wave which propagates at nearly constant velocity (v_s). By sampling the waves at various positions, the relative time (Δt) of the signals can be utilized to determine the location and absorption of the molecule (r) (figure 5.1). Lastly, either a 2D tomosynthesis algorithm or 3D filtered back-projection method is used to form an image[49]. Note, hemoglobin is the largest absorber of near infrared energy in the tissue, allowing for the imaging of hemoglobin concentration and the percentage of oxygenated hemoglobin (SaO_2) through near infrared spectroscopy.

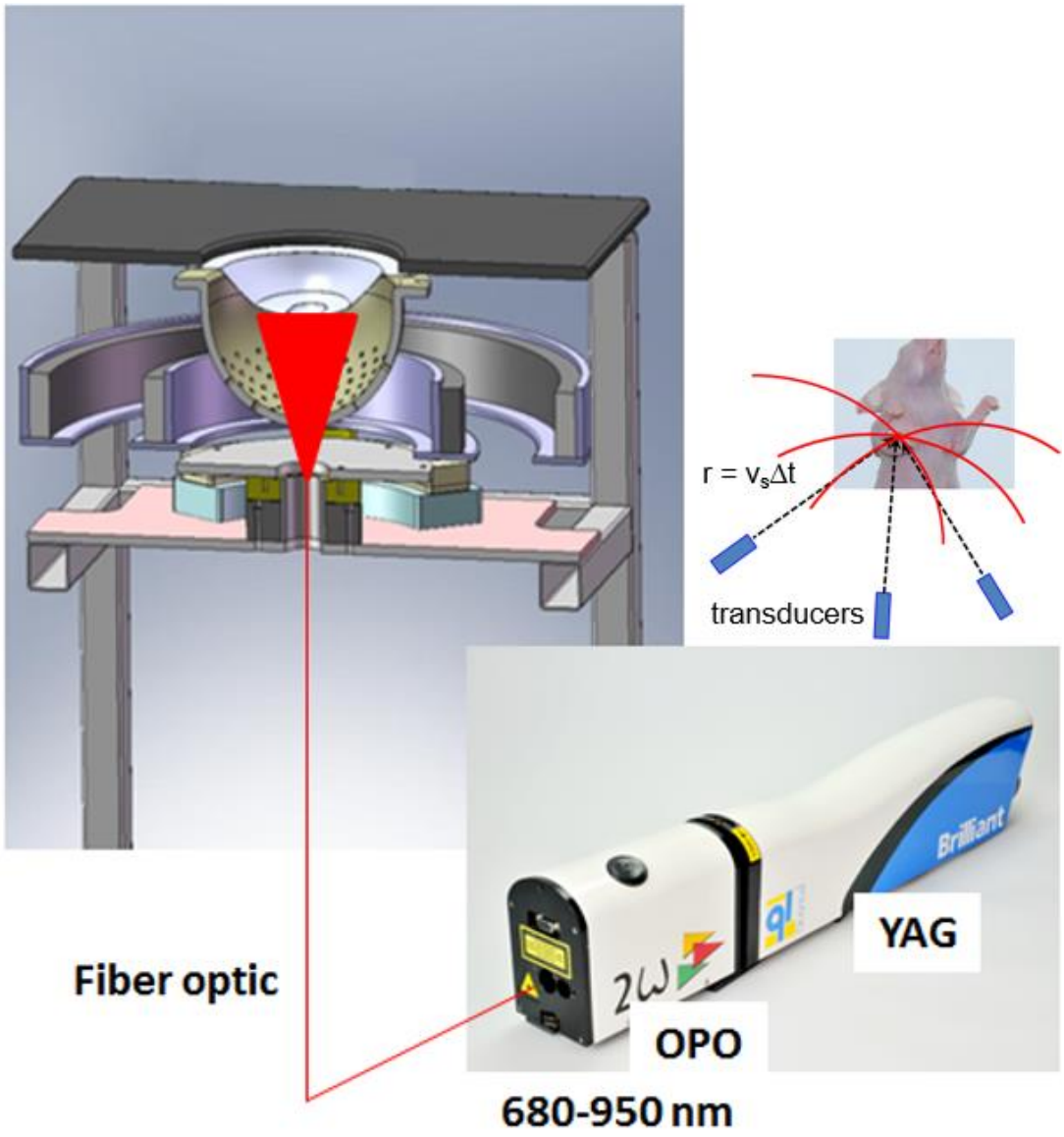

Figure 5.1 Photoacoustic principles. Pulsed laser energy is absorbed instantaneously into the tissue, causing the tissue to expand due to heating. The expanding tissues push against the surrounding tissue forming an acoustic (or ultrasonic) wave which propagates at nearly constant velocity (v_s). By sampling the waves at various positions, the relative time (Δt) of the signals can be utilized to determine the location and absorption of the molecule (r).

The goal of these experiments is to validate the relationship between SaO_2 and pO_2 in breast tumors in mice using photoacoustic computed tomographic imaging and OxyLite probe, respectively, and to determine the feasibility of translating this technology into a clinical setting. In its simplest form, the relationship between SaO_2 and pO_2 is described by the dissociation curve for hemolgobin, or Hill's equation, and is modeled as a sigmoidal curve that is a function of two parameters – the Hill coefficient, n, and the net association constant of HbO_2, K or p50 (or pO_2 at 50% SaO_2).

$$SaO_2 = \frac{(pO_2)^n}{K^n + (pO_2)^n} \tag{5.1}$$

First, a calibration study to validate Hill's equation in blood was performed by creating a closed circuit phantom to test the SaO_2 (682 Co-Oximeter System, Instrument Laboratory Inc., Ramsey, Minnesota) and pO_2 (Oxylite probe) relationship. Next, non-invasive localized measurements of SaO_2 in MDA-MD-231 and MCF7 breast tumors using PCT spectroscopic methods were compared to pO_2 levels in vivo.

5.2 Methods

5.2.1 Phantom Model

In Figure 5.2(A), a closed circuit system was constructed to simulate the flow of blood in a blood vessel. A tonometer was used to mix or bubble various concentrations of air and nitrogen in the blood by varying their relative partial pressures in order to control pO_2 and SaO_2 levels. A capillary pump was used to mix the gases throughout all the entire blood volume. The OxyLab Series E oxygen and temperature integrated probe was placed within the tonometer to measure the pO_2 (mmHg). The probe employs a

phosphorous quenching technique using fiber optics. The tip of the probe releases light, which excites the phosphor. The phosphor molecules release energy, which bonds to an oxygen molecule. The amount of O_2 is determined using the Stern-Volmer phosphorescence decay equation. The co-oximeter was used to measure the SaO_2 in a sample of blood (0.3-0.5 mL) extracted from the circuit. These two measurements were plotted and fit to Hill's equation to obtain K [mmHg] and n.

In the second experiment, the blood was circulated in FEP tubing through a phantom filled with water, and exposed to light produced from a YAG laser and OPO tuned to the wavelengths of 700 and 850 nm. An ultrasound transducer (or transducer array) was used to measure the photoacoustic signals. To determine the SaO_2, a system of linear equations was solved, which was based on the laser induced pressure signals.

$$[Hb] * \mu_{1,\lambda_1 Hb} + [HbO_2] * \mu_{1,\lambda_1 HbO_2} = \mu_{\lambda_1} \quad (5.2)$$

$$[Hb] * \mu_{2,\lambda_2 Hb} + [HbO_2] * \mu_{2,\lambda_2 HbO_2} = \mu_{\lambda_2} \quad (5.3)$$

These SaO_2 measurements were compared to the values obtained from the co-oximeter. Next, the phantom was then imaged with a 128 element linear transducer array and reconstructed using a delay and sum reconstruction algorithm.

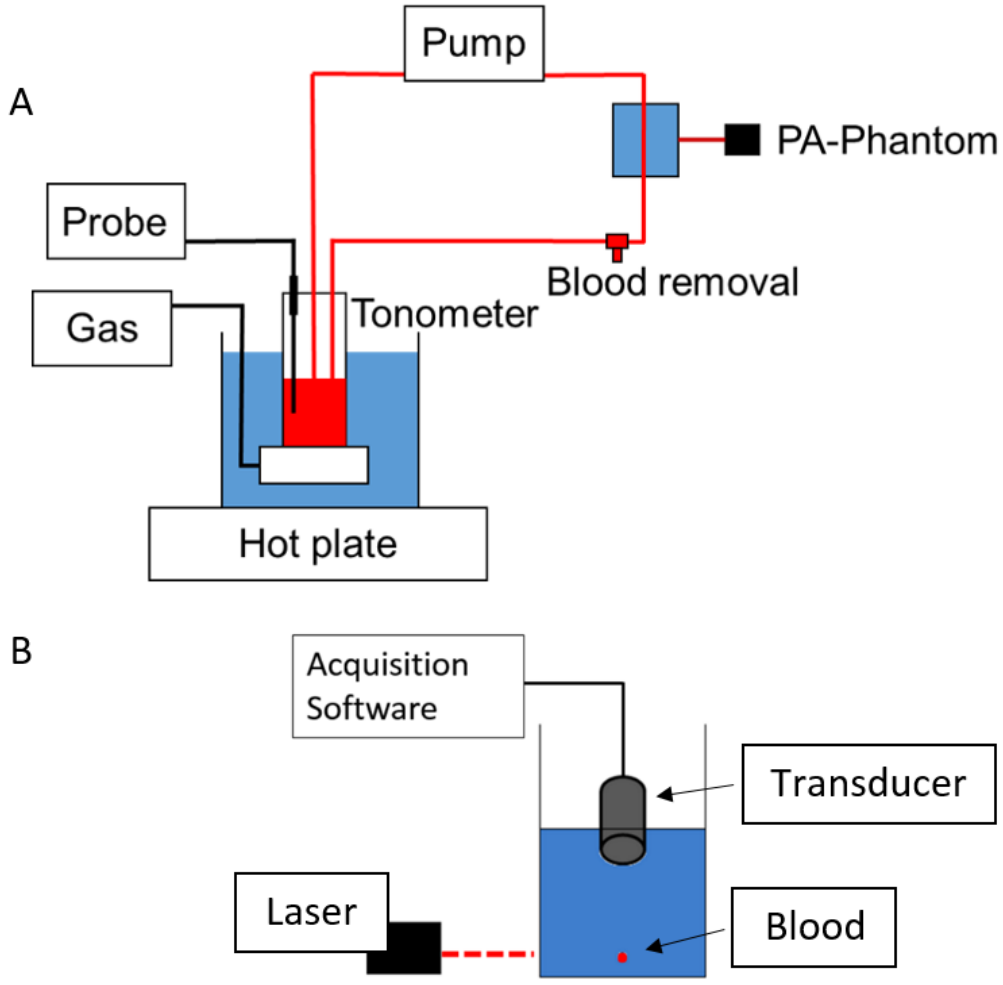

Figure 5.2 Blood circulation system design. A) Phantom setup B) photoacoustic spectroscopy setup. By inducing a pressure wave at two different wavelengths and recording the amplitude with an ultrasound transducer, the concentrations of oxy- and deoxyhemoglobin can be calculated by solving a system of linear equations

5.2.2 Mouse Model

MDA-MD231, MCF7 and MCF7/VEGF cells (1-5x10^6) were injected into the mammary fat pads of athymic nude mice. Tumors were allowed to reach a diameter of approximately 8-12 mm and then spectrally imaged within photoacoustic computed tomographic scanners (Small Animal Photoacoustic Scanner, Optosonics Inc., Indianapolis, IN). The Oxylite probe was used to measure the pO_2 values within these tumors by inserting a needle across the central axis of the tumor (using calipers) and then inserting the probe tip through a needle. Measurements were taken every 1 minute in 1 mm increments. Photoacoustic images prior to and after the probe was inserted into the tumor were used to determine the insertion path (line) of the probe from which the SaO_2 values were measured. Scatter plots of the SaO_2 and pO_2 values were fit to Hill's equation to obtain K and n using the curve fit tool in MATLAB™.

5.3 Results

5.3.1 Phantom Model

The measurements in our phantom yielded an n of 2.26 (2.09, 2.43 95% confidence interval) and K (p50) of 23.4 mmHg (22.5, 24.3 95% confidence interval) for a solution to Hill's equation,

$$SaO_2 = \frac{(pO_2)^{2.265}}{23.41^{2.265} + (pO_2)^{2.265}} \tag{5.2}$$

with an $R^2 = 0.997$ shown in Figure 5.3A. The SaO_2 calculations from the laser induced photoacoustic signals correlated very well with the co-oximeter measurements (R^2 =

0.981) above 65% SaO_2. The calculations diverged when the SaO_2 fell below 65%. The lowest photoacoustic measured SaO_2 was 57% whereas the co-oximeter measured 15%. The phased array reconstruction of the 1.1 mm wire filled with blood shown in Figure 5.4A has a FWHM of 1 mm in the axial direction and 2 mm in the lateral direction.

A

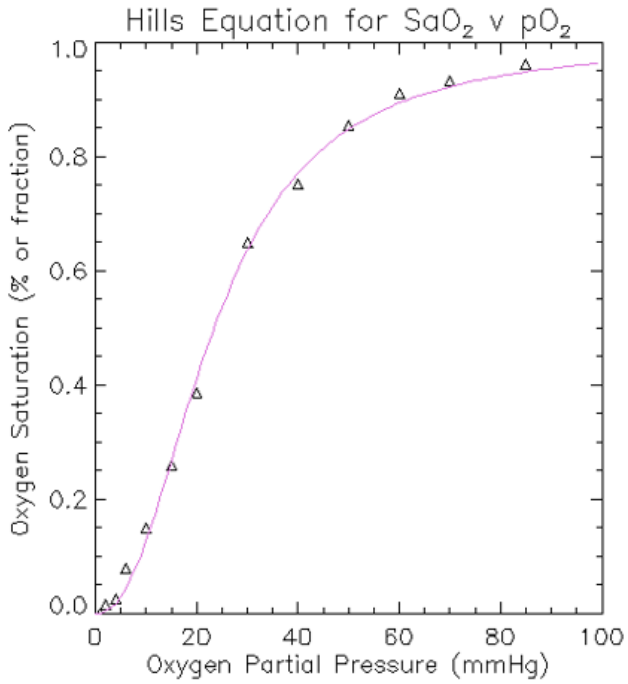

B

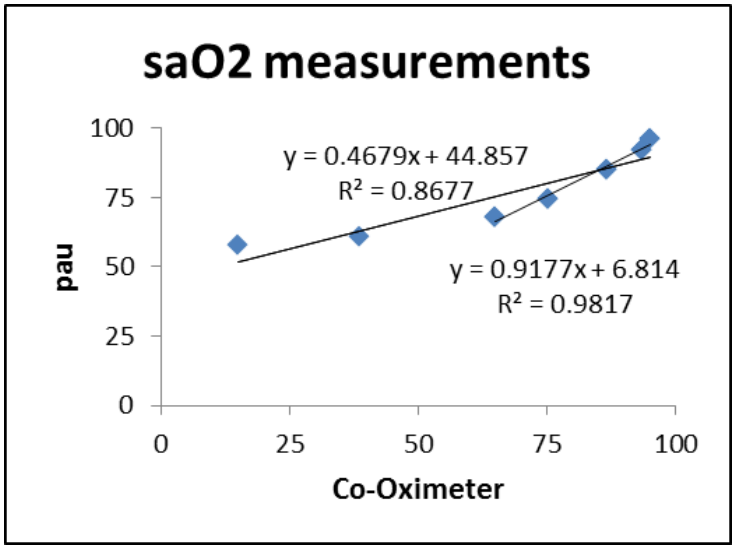

Figure 5.3 Phantom Results. A) Graph of calibration data (Δ) with Hill's equation fit line (magenta line). B) Photoacoustic vs. Co-oximeter measured SaO_2 values

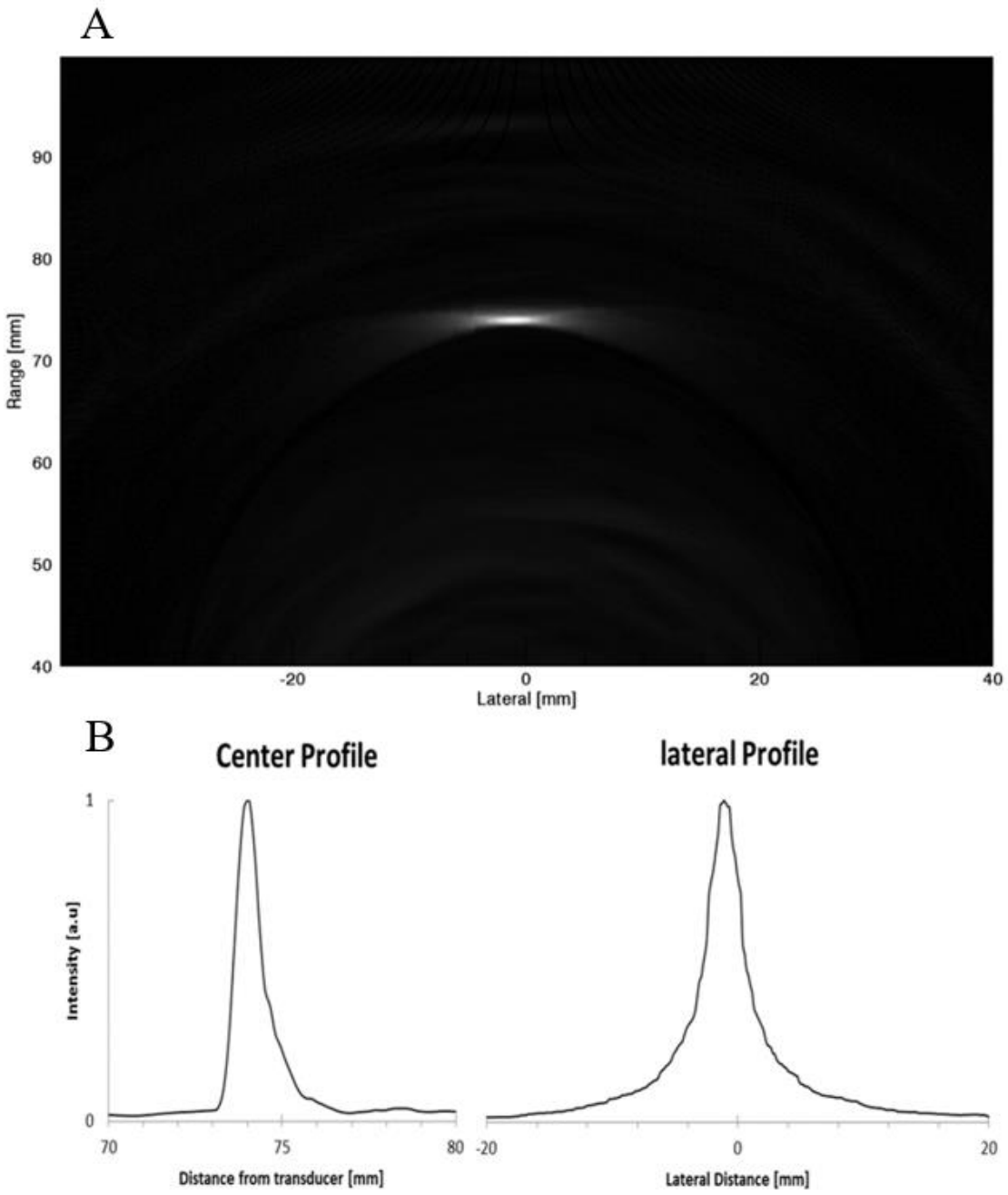

Figure 5.4 PA Image Reconstruction. A) Phased array photoacoustic reconstruction of 1.1 mm tube filled with blood. B) Intensity profiles

5.3.2 Mouse Model

The SaO_2 values along the insertion line of the OxyLite probe was determined by fitting the photoacoustic CT images spectral data to oxy- and deoxy-hemoglobin optical absorption curves.. Images showing the spectroscopy analysis are shown in Figure 5.5. In this example, the SaO_2 values for voxels of low, moderate, and high oxygenation were calculated with reduced chi squared values of 0.51 for a SaO_2 of 5.9%, 0.41 for 52.5% and 0.32 for 85%, representing good fits for a range of conditions. Plots of SaO_2 versus pO_2 were fit to Hill's equation to obtain K and n for both the MCF7 and MDA-MD-231 strains of breast cancer. The MCF7 data showed a reduced K value of 17.2 mmHg compared to the calibration curve (p50 of 23.5 mmHg) and 1.76 for Hill's coefficient. The data obtained from the MDA-MD-231 tumor measured a K value of 20.7 mmHg and 1.63 for the Hill coefficient.

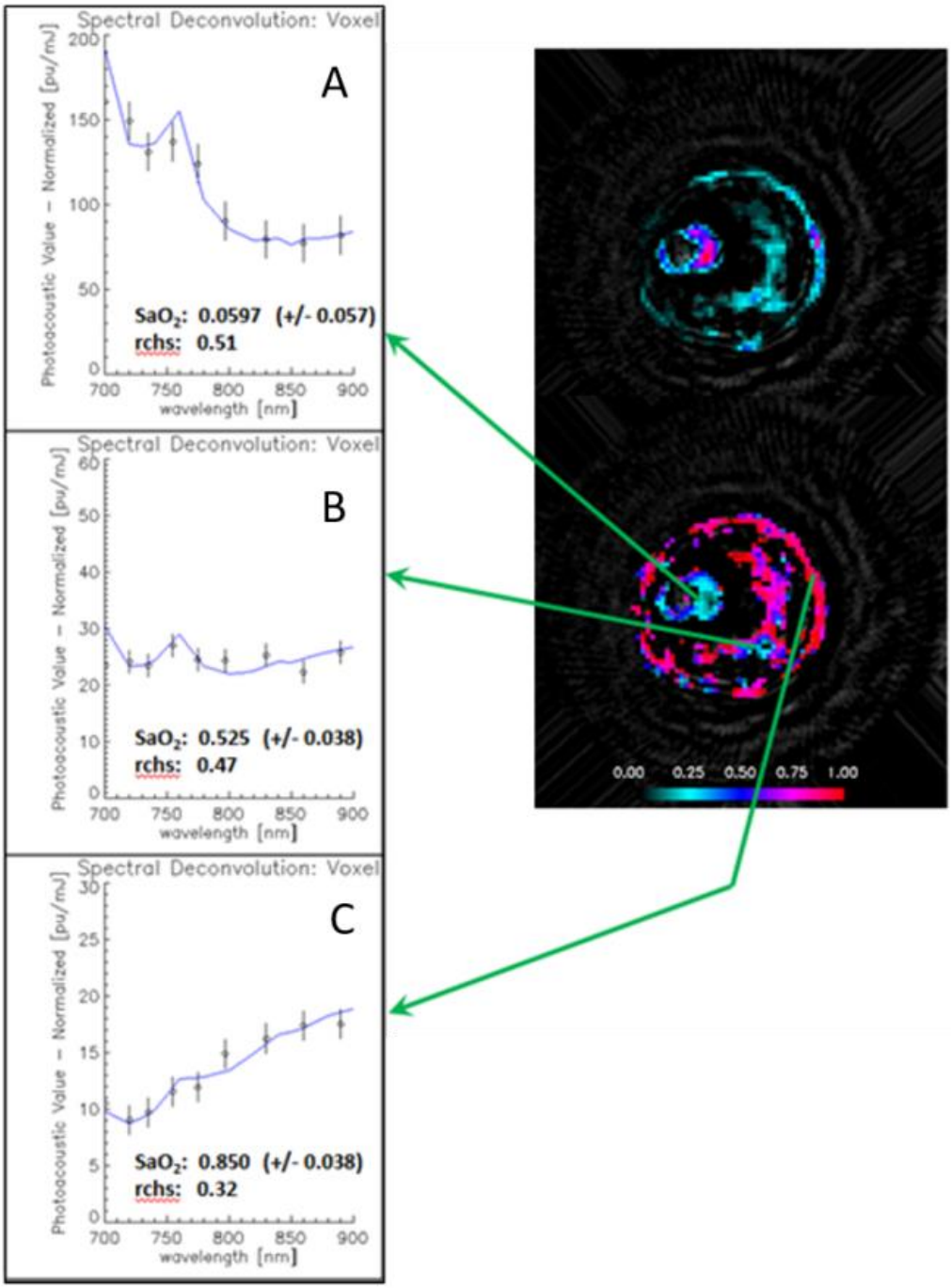

Figure 5.5 Spectroscopy analysis. The different graphs exemplify the oxygenation of the respective voxel in the image. They also display the respective SaO_2 values for each voxel. The image range from low oxygenation to high oxygenation in the following order: A, B, C.

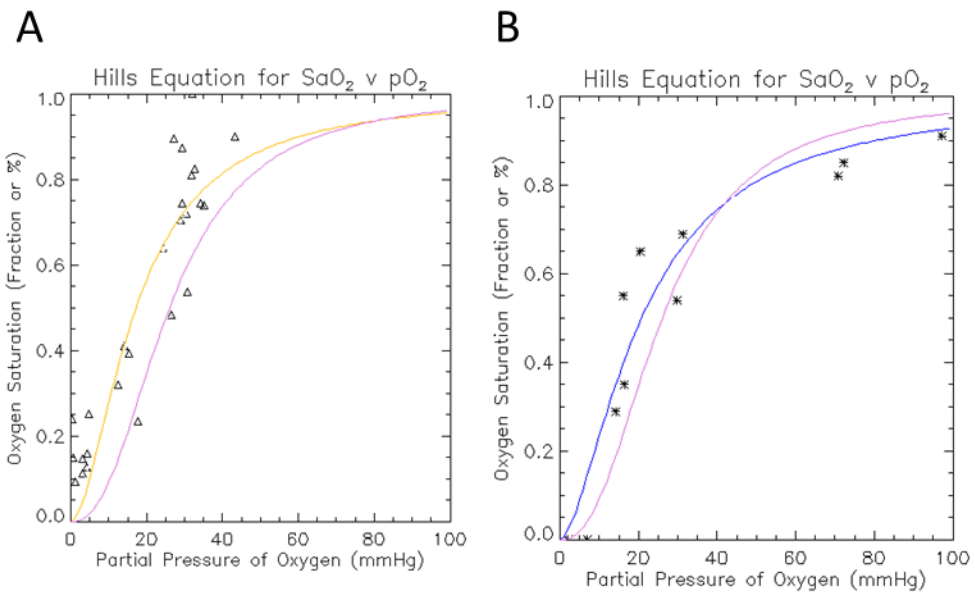

Figure 5.6 Dissociation curves for the mouse models**.** A) Graph displaying MCF7 data (Δ), the Hill's equation fit (gold line) and the calibration fit (magenta line). B) Graph displaying MDA-Md231 data (*), the Hill's equation fit (blue line) and the calibration fit (magenta line).

5.4 Discussion

The objective of this study was to calibrate and validate photoacoustic measurements of the local SaO_2 in tumors correlates to the oxygen concentration pO_2 as measured by the OxyLite probe (Gold Standard). Experiments were performed to measure both oxygen levels and oxygen saturation levels in blood within phantoms and tumors. First, a blood phantom was designed and used to successfully measure the dissociation curve for RBCs. Based on fits to Hill's equation, K (or P_{50}) of 23.4 mmHg and an n of 2.26 was determined, and within the expected range of 20-25 mmHg[50,51]. This same technique was applied in xenograft mouse models bearing MCF7 and MBA-MD-231 breast tumors, and measured a shift or lower P_{50} value in the dissociation curve. For MCF7 tumors, the K value was 5.8 mmHg lower compared to calibration blood curves, 17.2 mmHg compared to 23.4 mmHg. However, a number of factors can cause such a shift, such as temperature, pH, and DPG.

Given that tumors are known for acidosis (reduced pH), this shift is believed to be related to the pH formed within the tumor[52,53]. However, the K value for MDA-MB-231 is within the expected range at 20.7 mmHg. Acidosis is known to vary within a tumor and for different tumor types, and could explain these results; however, further analysis is necessary to assess significance and validate this hypothesis. For the parameter n, they were also lower than calibration values, 1.76 and 1.63 respectively. This suggests a variation in cooperative binding within hemoglobin, which appears unlikely[54]. As with K value, further statistical analysis is ongoing to determine if these differences are significant.

5.5 Conclusions

Overall, the results from this study demonstrate that PCT-S can provide measures of intra-tumor oxygenation. To date, these are the first known measurements comparing the SaO_2 levels obtained from photoacoustic imaging to a gold standard for pO_2. However, some issues remain: difference in K and n to that of the calibration curve, and scatter in the data.

Our next step is to reduce the uncertainty (systematic and statistical) in the data. An important factor is the variation in the photon fluence based on radiative transport of the laser light through the tumor. Given that the light at a point deep within a tumor depends on the absorption properties of the tumor prior to reaching this point, systematic errors in the spectral data can occur and need to be corrected. Similarly, image artifacts due to incomplete sampling can influence spectral data and will need to be corrected. Finally, devising a technique to better determine the location of the probe passes through the tumor will help reduce scatter in the data.

CHAPTER 6. DISCUSSION

Although the work was targeted around canine TCC, applications can include many abdominal cancers shown to have favorable outcomes with radiation therapy. The American Cancer Society predicts over 150,000 deaths from cancer of the digestive tract, over 30,000 deaths from cancer of the urinary system and over 40,000 deaths from breast cancer in 2016[55]. Although CBCT is the standard patient positioning technique, this work builds on the literature promoting ultrasound to be a viable option for image-guided RT. Specifically, for clinics that do not have a linear accelerator with CBCT capabilities and are not willing or not able to buy commercially available equipment.

Convincing clinics that do utilize kV imaging systems and CBCT for many of their treatment protocols to switch to US will be a tall order. Many of the diseases occur in elderly patients where the long-term, cumulative imaging dose is not a concern. The latency period, defined as the time from initial exposure to occurrence of malignancy induced by radiation was estimated to be between 5 and 15 years[56]. One group that would greatly benefit from a non-radiographic imaging modality is pediatrics, especially as treatments improve and the life expectancy post cancer moves beyond the latency period. An estimated 10,380 children (aged 1 to 14) will be diagnosed with cancer, with 1,250 expected to die from the disease[55]. Finding data on the dose delivered from the many different radiographic imaging modalities has proven difficult. Different imaging modalities deliver very

unique spatial distributions of dose. Consequently, the physiological risks can be considerably different[9]. Work on assessing patient organ doses resulting from CBCT has become an area of active research[57]. The most efficient way to remove concerns of risk from imaging dose is to remove as much as the imaging dose as possible from the procedure. Ultrasound provides a viable alternative.

In addition to removing the imaging dose from patient setup, US can provide intrafractional monitoring of organ motion throughout treatment without the use of ionizing radiation or implanted fiducial markers. Intrafractional monitoring of organ motion is critical to delivering the correct dose to the target as well as not over irradiating the healthy surrounding tissue. The investigation of internal organ motion, deformation, and the dosimetric impact of these changes has been studied and summarized[58]. Concluding that the changes are significant and that intrafractional monitoring of the changes may be necessary.

Until recently, non-radiographic localization systems have been limited to infrared cameras, implanted radiofrequency and ultrasound[9]. The literature reports that using infrared cameras for surface tracking is a poor surrogate for prostate motion[59,60] and the correlation with disease sites in the thorax and abdomen is inconclusive. Radiofrequency devices need to be implanted, which can be invasive. Additionally, they still don't truly report organ motion, only movement of the device, which may not give a clear picture of the internal anatomy. Using MRI is a new technique for IGRT. As more systems get installed, data on the functionality and limitations will become available. Looking forward, we will have to wait see if being limited to a cobalt-60 source and not

having access to an electron beam significantly affect the widespread adoption of these systems.

The advantage of ultrasound is the ability to image internal anatomy without the use of ionizing radiation or implanted devices. Our system specifically addresses deficiencies in currently available systems, such as free-hand probe manipulation, and designed with the ability to incorporate a fluid filled bolus to remove distortions caused by probe pressure. Where our system doesn't match those that are commercially available at this time is the online communication with record and verify systems to utilize the intrafractional organ motion. Software development that is beyond the purpose of this study will be necessary to include these features.

Given the translational validation of the US for clinical treatment of canine patients, our focus is toward the feasibility of using PCT to provide new imaging properties and link this to tumor radiation sensitivity and immune response of the patient. The goal being to be able to provide structural and functional information, much like PET/CT, but without the use of any ionizing radiation and in a way that can be incorporated into the radiation therapy suite. Angiogenesis, the production of new blood vessels is considered to be one of the integral hallmarks of cancer[61]. The presence of hypoxia and cell proliferation rate, features unique to the tumor, are important factors in radiation treatment response[62].

The results from the PCT-S demonstrate that PCT-S can provide measures of intra-tumor oxygenation. To date, these are the first known measurements comparing photoacoustic SaO_2 to a gold standard for pO_2. Additionally, the resolution in our preclinical phantom measurements was better using a phased array reconstruction for

linear transducers (FWHM of 1 mm in axial, 2 mm in lateral) than PET (≈5 mm)[63] and SPECT (>15 mm)[64]. These measurements open up the door for imaging the heterogeneity of the tumor with high resolution. Dose painting is the prescription of a non-uniform dose distribution based on function information relating to the radio-resistant or radio-sensitive regions of the tumor. The hypothesis being, 1) the micro-environment of the tumor contains radio-resistant regions that lead to recurrence, 2) molecular and functional imaging of these regions will allow for mapping the heterogeneity of the tumor and 3) boosts to these regions will improve tumor control without increasing radiation induced toxicity[65].

Problems with implementing PET and SPECT for dose painting arise from the poor inherent resolution of the systems and an unacceptable dose to the patient from repeated scans. Photoacoustic imaging may provide the resolution necessary to properly visualize the radio-resistant regions of the tumor and because no radiation dose is associated with this technique, multiple scans can be acquired to monitor the change in the tumor microenvironment. Additional design considerations include the future use of ultrasound-based functionality (photoacoustics, radioacoustics, Doppler) to monitor blood flow[46] and hypoxia[47] and/or in-vivo dosimetry for applications in other therapeutic techniques, such as hyperthermia, anti-angiogenesis and particle therapy[48].

Another unique application of photoacoustics is in particle therapy. The bragg peak associated with particle therapy creates a similar pressure wave that can be measured as a function of absorbed dose. This provides a novel technique for in-vivo dosimetry[48], a major concern with the sharp dose gradients associated with particle therapy. Only recently has CBCT made its way into proton therapy treatment rooms. The

high temporal resolution of US, molecular PA imaging and treatment planning combined with in-vivo dosimetry has yet to be accomplished and has the ability to revolutionize radiation therapy.

As mentioned earlier, In-vivo models including complete physiologic processes such as multiple organ interactions, angiogenesis and the immune system are necessary to improve current in-vitro models[3]. It is critical to understand that the response to treatment in terms of tumor control and toxicity is often unique to individual patients. It has been shown that the expression of particular molecules in the tumor can be linked with either predicting certain outcomes from treatments or a change in prognoses[66,67].

The general hypothesis is that blood cytokine levels present prior to RT and during the course of treatment will be correlated with tumor control. We conducted a pilot study (N=3) investigating the production of cytokines in response to RT (complete data in Appendix B). Baseline cytokine levels comparing our control group (patients in the hospital for orthopedic evaluation) to our cancer subjects can be seen in Table 6.1. We found concentrations of Interleukin(IL)-10 (anti-inflammatory) to be significantly reduced ($p=0.05$) in cancer patients than control, whereas IL-8 (inflammation and hypoxia), Monocyte Chemoattractant Protein (MCP)-1 (regulates monocytes/macrophages) and Chemokine Ligand (CXCL)-1 (also known as KC-like, angiogenesis) to be significantly increased in the cancer patients compared to control. Many of the cytokines we investigated are associated with inflammation and angiogenesis, biomarkers that can be used to validate the efficacy of dose painting and radiation therapy in general.

Table 6.1. Mean control and cancer patients before treatment with the ranges (min-max) shown in parentheses

	Control	**Baseline**
IL-10	61.38* (0-178.35)	25.33 (8.7-55.61)
IL-2	0	0
IL-6	11.05 (0.27-28.39)	3.23 (0-5.9)
IL-8	4907.3 (3523.75-7241.35)	8717.77* (5016.12-13481.01)
MCP-1	89.23 (0-267.68)	220.77* (0-402.4)
TNF-α	0	0
KC	651.92 (351.35-1197.58)	1480.43* (592.41-2811.42)

*P=0.05

CHAPTER 7. CONCLUSIONS AND FUTURE DIRECTIONS

The overall purpose of the first part of this work was to present methods for developing an ultrasound guidance system solely on equipment available to nearly all institutions. Although US yielded poorer resolutions than CBCT, the theoretical uncertainty, taking into account all the underlying physical principles of US, beam formation, and artifacts, still allowed us to register US to CT with errors under the 2 mm recommendation.

Based on our results, the initial hypothesis that US would reduce the uncertainty in delineating tumor margins remains unsolved. Experiments modeling deformable registration and intrafactional motion will be necessary to conclude whether smaller planning target volumes can be applied to the bladder. The work builds on the literature promoting ultrasound to be a viable option for image-guided RT, specifically for clinics not willing or not able to buy commercially available equipment. As is the case at the Purdue University Teaching Hospital, where patients with bladder cancer are not eligible for RT because of the inability to accurately visualize the bladder at patient setup. Additionally, the procedures for importing images and volumes into the treatment planning system has not been previously reported. These methods will allow future studies to investigate the use of other imaging modalities in a treatment planning environment.

As with any engineering endeavor, the development never ends. Future work should address the brittleness of the acrylic components. Ideally, the next design should be built from carbon fiber. A more robust prototype will facilitate long-term acceptance testing, where spatial reproducibility and drift can be assessed. Assuming those pass, only the development of communication with record and verify systems will be necessary to implement this technology.

The second half of this study investigated the use of photoacoustic tomography to identify intra-tumor hypoxic variations impacting radiation response and outcome. Overall, the results from this study demonstrate that PCT-S can provide measures of intra-tumor oxygenation. To date, these are the first known measurements comparing photoacoustic SaO_2 to a gold standard for pO2. However, some issues remain: difference in K and n to that of the calibration curve, and scatter in the data.

Our next step is to reduce the uncertainty (systematic and statistical) in the data. An important factor is the variation in the photon fluence based on radiative transport of the laser light through the tumor. Given that the light at a point deep within a tumor depends on the absorption properties of the tumor prior to reaching this point, systematic errors in the spectral data can occur and need to be corrected. This is will be a challenging task as the technology moves from small to larger animals to humans. In addition, implementing a reconstruction algorithm based on a linear US transducer array will be necessary to truly fuse the anatomical and functional imaging to a single modality.

The final phase of this study was to evaluate the production of cytokines in canine patients with fully intact immune systems and spontaneous cancer, much like the way

cancer effects human patients. Potentially identifying advantageous cycling of radio-sensitivity and/or radio-resistance during the course of RT.

REFERENCES

REFERENCES

1. Knapp, D.W. & Waters, D.J. Naturally occurring cancer in pet dogs: important models for developing improved cancer therapy for humans. *Molecular medicine today* **3**, 8-11 (1997).

2. Muren, L.P., Smaaland, R. & Dahl, O. Organ motion, set-up variation and treatment margins in radical radiotherapy of urinary bladder cancer. *Radiotherapy and oncology : journal of the European Society for Therapeutic Radiology and Oncology* **69**, 291-304 (2003).

3. Knapp, D.W., *et al.* Naturally-occurring canine transitional cell carcinoma of the urinary bladder A relevant model of human invasive bladder cancer. *Urologic oncology* **5**, 47-59 (2000).

4. Chamberlain, W.E. & Young, B.R. Should the Method of Coutard be Applied in All Cases of Cancer Treated by Roentgen Rays? *Radiology* **29**, 186-189 (1937).

5. Dawson, L.A. & Sharpe, M.B. Image-guided radiotherapy: rationale, benefits, and limitations. *The Lancet Oncology* **7**, 848-858 (2006).

6. Xing, L., *et al.* Overview of image-guided radiation therapy. *Medical dosimetry : official journal of the American Association of Medical Dosimetrists* **31**, 91-112 (2006).

7. van Elmpt, W., *et al.* A literature review of electronic portal imaging for radiotherapy dosimetry. *Radiotherapy and oncology : journal of the European Society for Therapeutic Radiology and Oncology* **88**, 289-309 (2008).

8. Langmack, K.A. Portal imaging. *The British journal of radiology* **74**, 789-804 (2001).

9. Murphy, M.J., *et al.* The management of imaging dose during image-guided radiotherapy: report of the AAPM Task Group 75. *Medical physics* **34**, 4041-4063 (2007).

10. Choyke, P.L., Knopp, M.V. & Libutti, S.K. Special Techniques for Imaging Blood Flow to Tumors. *The Cancer Journal* **8**, 109-118 (2002).

11. Choyke, P.L., Dwyer, A.J. & Knopp, M.V. Functional tumor imaging with dynamic contrast-enhanced magnetic resonance imaging. *Journal of magnetic resonance imaging : JMRI* **17**, 509-520 (2003).

12. Wang, L.V. Prospects of photoacoustic tomography. *Medical physics* **35**, 5758-5767 (2008).

13. Minafra, L. & Bravatà, V. Cell and molecular response to IORT treatment. *Translational Cancer Research* **3**, 32-47 (2014).

14. Balkwill, F. & Mantovani, A. Inflammation and cancer: back to Virchow? *Lancet (London, England)* **357**, 539-545 (2001).

15. Brigati, C., Noonan, D.M., Albini, A. & Benelli, R. Tumors and inflammatory infiltrates: friends or foes? *Clinical & experimental metastasis* **19**, 247-258 (2002).

16. Caruso, C., Lio, D., Cavallone, L. & Franceschi, C. Aging, longevity, inflammation, and cancer. *Annals of the New York Academy of Sciences* **1028**, 1-13 (2004).

17. Grivennikov, S.I. Immunity, Inflammation, and Cancer. **140**, 883-899 (2010).

18. Lucignani, G., Jereczek-Fossa, B.A. & Orecchia, R. The role of molecular imaging in precision radiation therapy for target definition, treatment planning optimisation and quality control. *European journal of nuclear medicine and molecular imaging* **31**, 1059-1063 (2004).

19. Carmeliet, P. & Jain, R.K. Angiogenesis in cancer and other diseases. *Nature* **407**, 249-257 (2000).

20. Bushberg, J.T. *The Essential Physics of Medical Imaging*, (Lippincott Williams & Wilkins, Philadelphia, 2002).

21. Kinahan, P. Ultrasound [PDF document]. (Retrieved from Lecture Notes Online Website: http://courses.washington.edu/bioen508/Lecture6-US.pdf, 2006).

22. Tucholski, E. Waves and the One-Dimensional Wave Equation [pdf]. (2007).

23. Ng, A. & Swanevelder, J. Resolution in ultrasound imaging. *Continuing Education in Anaesthesia, Critical Care & Pain* **11**, 186-192 (2011).

24. Feldman, M.K., Katyal, S. & Blackwood, M.S. US Artifacts. *RadioGraphics* **29**, 1179-1189 (2009).

25. Woodard, H.Q. & White, D.R. The composition of body tissues. *The British journal of radiology* **59**, 1209-1218 (1986).

26. Al-Kaabi, Y.N.A.-N.A.M.A.-J.M.A.K.S.A. Functional Dependence of Ultrasonic Speed in Water on Salinity and Temperature. *Nondestructive Testing (NDT)* **11**(2006).

27. Tanoue, H., Hagiwara, Y., Kobayashi, K. & Saijo, Y. Ultrasonic tissue characterization of prostate biopsy tissues by ultrasound speed microscope. *Conference proceedings : ... Annual International Conference of the IEEE Engineering in Medicine and Biology Society. IEEE Engineering in Medicine and Biology Society. Annual Conference* **2011**, 8499-8502 (2011).

28. Chan, M., *et al.* Evaluation of imaging performance of major image guidance systems. *Biomedical Imaging and Intervention Journal* **7**(2011).

29. Bylund, K.C., *et al.* Analysis of interfraction prostate motion using megavoltage cone beam computed tomography. *International journal of radiation oncology, biology, physics* **72**, 949-956 (2008).

30. Gayou, O. & Miften, M. Comparison of mega-voltage cone-beam computed tomography prostate localization with online ultrasound and fiducial markers methods. *Medical physics* **35**, 531-538 (2008).

31. Fontanarosa, D., van der Meer, S., Harris, E. & Verhaegen, F. A CT based correction method for speed of sound aberration for ultrasound based image guided radiotherapy. *Medical physics* **38**, 2665-2673 (2011).

32. Fontanarosa, D., *et al.* A speed of sound aberration correction algorithm for curvilinear ultrasound transducers in ultrasound-based image-guided radiotherapy. *Physics in medicine and biology* **58**, 1341-1360 (2013).

33. Lediju Bell, M.A., Sen, H.T., Iordachita, I., Kazanzides, P. & Wong, J. In vivo reproducibility of robotic probe placement for a novel ultrasound-guided radiation therapy system. *JMIOBU* **1**, 025001-025001 (2014).

34. Sen, H.T., Bell, M.A.L., Iordachita, I., Wong, J. & Kazanzides, P. A cooperatively controlled robot for ultrasound monitoring of radiation therapy. in *Intelligent Robots and Systems (IROS), 2013 IEEE/RSJ International Conference on* 3071-3076 (2013).

35. Chadha, M., Young, A., Geraghty, C., Masino, R. & Harrison, L. Image guidance using 3D-ultrasound (3D-US) for daily positioning of lumpectomy cavity for boost irradiation. *Radiation Oncology (London, England)* **6**, 45 (2011).

36. Fraser, D.J., *et al.* Dosimetric consequences of misalignment and realignment in prostate 3DCRT using intramodality ultrasound image guidance. *Medical physics* **37**, 2787-2795 (2010).

37. Western, C., Hristov, D. & Schlosser, J. Ultrasound Imaging in Radiation Therapy: From Interfractional to Intrafractional Guidance. *Cureus* **7**, e280 (2015).

38. Jones, F.E. & Harris, G.L. ITS-90 Density of water formulation for volumetric standards and calibration. *Journal of Research of the National Institute of Standards and Technology* **97**, 335-340 (1992).

39. Greenspan, M. & Tschiegg, C.E. Tables of the Speed of Sound in Water. *The Journal of the Acoustical Society of America* **31**, 75-76 (1959).

40. O'Brien, W.D., Jr., Olerud, J., Shung, K.K. & Reid, J.M. Quantitative acoustical assessment of wound maturation with acoustic microscopy. *J Acoust Soc Am* **69**, 575-579 (1981).

41. T. Bowen, W.G.C., R.L. Nasoni, A.E. Pifer, R.R. Sholes. *Measurment of the temperature dependence of the velocity of ultrasound in soft tissues*, (National Measurement Laboratory National Bureau of Standards, Washington, DC, 1979).

42. Klein, E.E., *et al.* Task Group 142 report: Quality assurance of medical acceleratorsa). *Medical physics* **36**, 4197-4212 (2009).

43. Emma, J.H., Naomi, R.M., Jeffrey, C.B., Symonds-Tayler, J.R.N. & Philip, M.E. Speckle tracking in a phantom and feature-based tracking in liver in the presence of respiratory motion using 4D ultrasound. *Physics in medicine and biology* **55**, 3363 (2010).

44. Tuathan, P.O.S., *et al.* 4D ultrasound speckle tracking of intra-fraction prostate motion: a phantom-based comparison with x-ray fiducial tracking using CyberKnife. *Physics in medicine and biology* **59**, 1701 (2014).

45. Abramowitz, M.C., *et al.* Noninvasive Real-time Prostate Tracking Using a Transperineal Ultrasound Approach. *International Journal of Radiation Oncology • Biology • Physics* **84**, S133.

46. Pilatou, M.C., Marani, E., de Mul, F.F. & Steenbergen, W. Photoacoustic imaging of brain perfusion on albino rats by using evans blue as contrast agent. *Archives of physiology and biochemistry* **111**, 389-397 (2003).

47. Li, M.L., *et al.* Simultaneous Molecular and Hypoxia Imaging of Brain Tumors <emphasis emphasistype="italic">In Vivo</emphasis> Using Spectroscopic Photoacoustic Tomography. *Proceedings of the IEEE* **96**, 481-489 (2008).

48. Alsanea, F., Moskvin, V. & Stantz, K.M. Feasibility of RACT for 3D dose measurement and range verification in a water phantom. *Medical physics* **42**, 937-946 (2015).

49. Kruger, R.A., Liu, P., Fang, Y.R. & Appledorn, C.R. Photoacoustic ultrasound (PAUS)—Reconstruction tomography. *Medical physics* **22**, 1605-1609 (1995).

50. O'Riordan, J.F., Goldstick, T.K., Ditzel, J. & Ernest, J.T. Characterization of oxygen-hemoglobin equilibrium curves using nonlinear regression of the Hill equation: parameter values for normal human adults. *Advances in experimental medicine and biology* **159**, 435-444 (1983).

51. Yonenaga, K., Todoroki, H., Tokunaga, K. & Hamasaki, N. Changes in adenosine triphosphate, 2,3 diphosphoglycerate, and P50 of dog blood following transfusion of autologous red cells pretreated with phosphoenolpyruvate in vitro. *Transfusion* **26**, 194-198 (1986).

52. Montcourrier, P., Silver, I., Farnoud, R., Bird, I. & Rochefort, H. Breast cancer cells have a high capacity to acidify extracellular milieu by a dual mechanism. *Clinical & experimental metastasis* **15**, 382-392 (1997).

53. Chiche, J., Brahimi-Horn, M.C. & Pouyssegur, J. Tumour hypoxia induces a metabolic shift causing acidosis: a common feature in cancer. *Journal of cellular and molecular medicine* **14**, 771-794 (2010).

54. Heck, H.d.A. Statistical theory of cooperative binding to proteins. Hill equation and the binding potential. *Journal of the American Chemical Society* **93**, 23-29 (1971).

55. Siegel, R.L., Miller, K.D. & Jemal, A. Cancer statistics, 2016. *CA: A Cancer Journal for Clinicians* **66**, 7-30 (2016).

56. Sountoulides, P., Koletsas, N., Kikidakis, D., Paschalidis, K. & Sofikitis, N. Secondary malignancies following radiotherapy for prostate cancer. *Therapeutic Advances in Urology* **2**, 119-125 (2010).

57. Rampado, O., *et al.* Evaluation of various approaches for assessing dose indicators and patient organ doses resulting from radiotherapy cone-beam CT. *Medical physics* **43**, 2515-2526 (2016).

58. Keall, P.J., *et al.* The management of respiratory motion in radiation oncology report of AAPM Task Group 76. *Medical physics* **33**, 3874-3900 (2006).

59. Crook, J.M., Raymond, Y., Salhani, D., Yang, H. & Esche, B. Prostate motion during standard radiotherapy as assessed by fiducial markers. *Radiotherapy and oncology : journal of the European Society for Therapeutic Radiology and Oncology* **37**, 35-42 (1995).

60. Ramsey, C.R., *et al.* Image-guided helical tomotherapy for localized prostate cancer: technique and initial clinical observations. *Journal of applied clinical medical physics / American College of Medical Physics* **8**, 2320 (2007).

61. Hanahan, D. & Weinberg, Robert A. Hallmarks of Cancer: The Next Generation. *Cell* **144**, 646-674 (2011).

62. Munley, M.T., *et al.* An introduction to molecular imaging in radiation oncology: a report by the AAPM Working Group on Molecular Imaging in Radiation Oncology (WGMIR). *Medical physics* **40**, 101501 (2013).

63. Saha, G.B. *Basics of PET Imaging: Physics, Chemistry, and Regulations*, (Springer, New York, NY, 2005).

64. Groch, M.W. & Erwin, W.D. SPECT in the year 2000: basic principles. *Journal of nuclear medicine technology* **28**, 233-244 (2000).

65. Bentzen, S.M. & Gregoire, V. Molecular imaging-based dose painting: a novel paradigm for radiation therapy prescription. *Seminars in radiation oncology* **21**, 101-110 (2011).

66. Zheng, Z., *et al.* DNA synthesis and repair genes RRM1 and ERCC1 in lung cancer. *The New England journal of medicine* **356**, 800-808 (2007).

67. Bepler, G., *et al.* RRM1 modulated in vitro and in vivo efficacy of gemcitabine and platinum in non-small-cell lung cancer. *J Clin Oncol* **24**, 4731-4737 (2006).

APPENDICES

Appendix A Phantom Artifacts

Improvements in ultrasound (US) image fidelity are needed to target features of radioresistance and radiosensitivity. Additionally, the accuracy and precision of 3D ultrasound guided radiation therapy (US-GRT) may be improved by enhancing the image quality of US images. A number of US artifacts; such as speckle, reverberation, refraction and speed of sound displacement, were exaggerated in our phantom compared to clinical images and attempts to remove, reduce or quantify these artifacts are presented in this section. For each of these factors, the data acquired from chapter 4 will be analyzed. We believe the position of the target in the FOV plays a critical role on what artifacts are seen. We know that refraction and the speed-of-sound will distort the image. The idea is to correct each method-of-distortion independently. All of the image processing was done in MATLAB^{TM} and details on the individual functions and filters can be on their website.

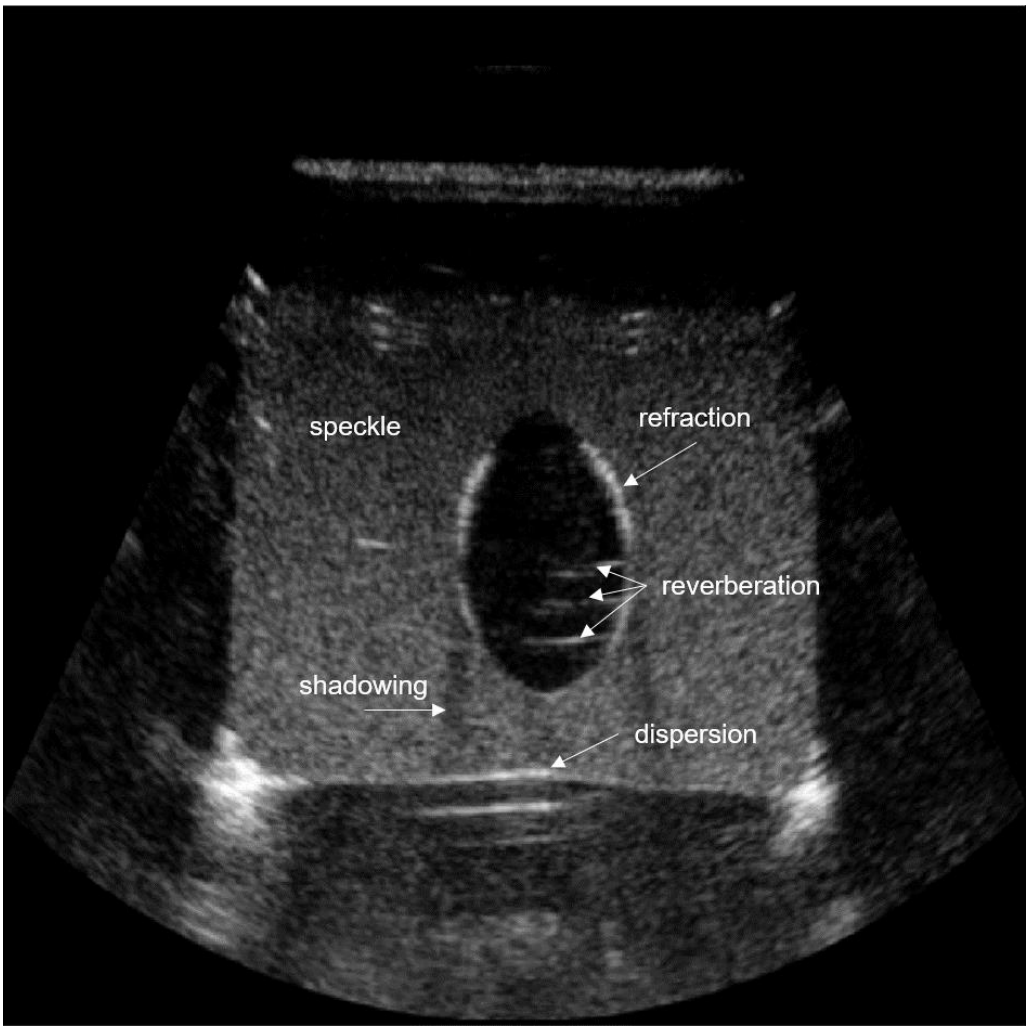

Figure A.1 Phantom Artifacts. Image of phantom showing different artifacts identified.

First, the built in wiener function in MATLAB^{TM} was used to reduce speckle. The function ‘wiener2’ lowpass-filters a grayscale image that has been degraded white noise. Wiener2 estimates the local mean and variance around each pixel. We found that a 10-by-10 region provided the best outcome. This function smooths the speckle noise while preserving high frequency edges. Secondly, the vertical intensity profiles for each image slice were digitally high-pass filtered. We used the MATLAB function y = filtfilt(b,a,x) to digitally filter our data by processing the input data, x, in both the forward and reverse directions to cancel out the phase shift added to signals only processed in the forward direction.

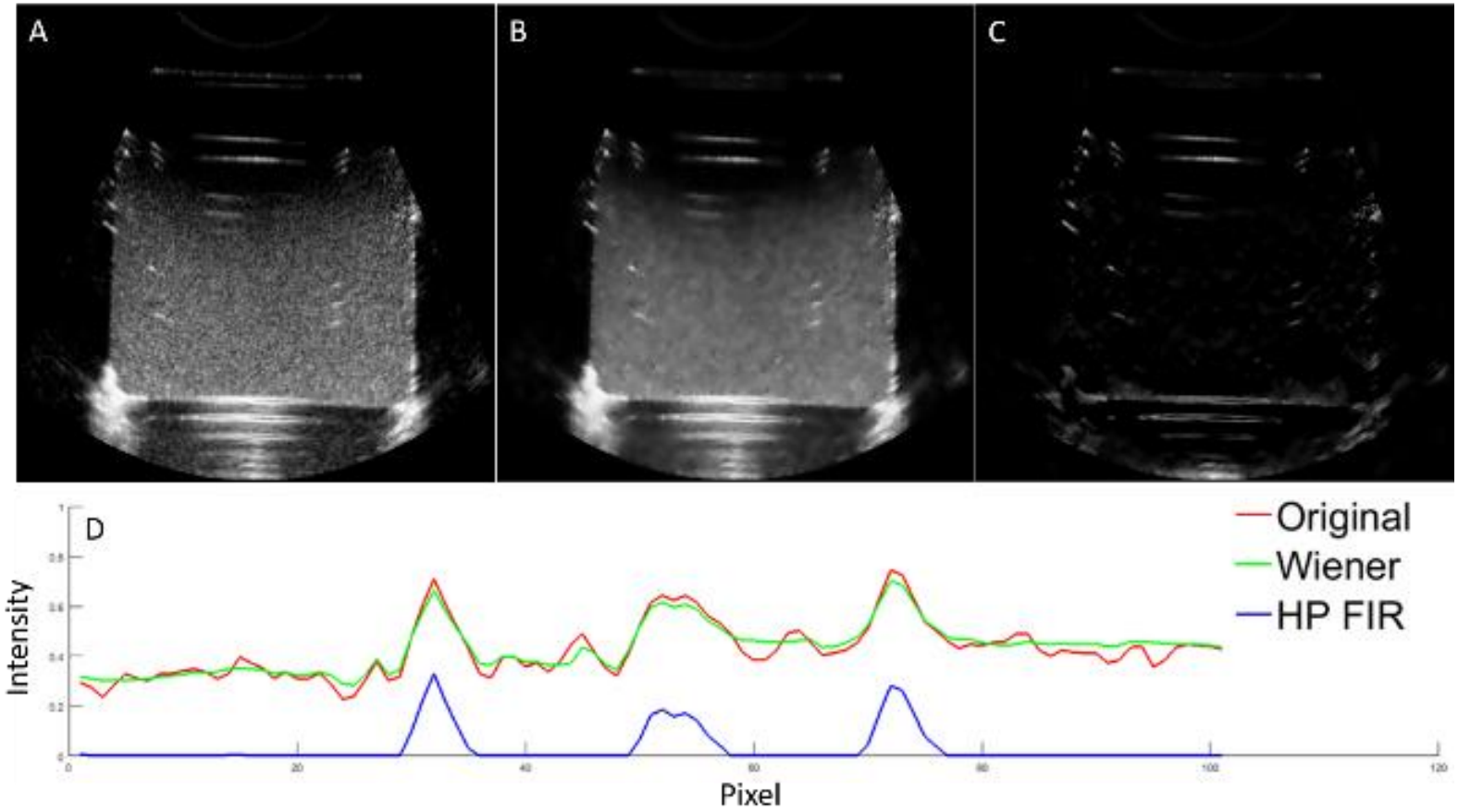

Figure A.2 Speckle reduction. The original (A), the wiener filtered (B) and the high-pass FIR filtered (C) images are shown. The speckle background noise is visibly smoother while the high frequency objects are preserved. Intensity profiles (D) through the three high-frequency objects in the right center are shown.

The next step was to remove the reverberation artifacts. Each image was normalized to have intensity values from 0-1. By definition, the reverberation artifact will have the same frequency as the original features. Therefore, we can set a region of interest around the artifacts and apply a fourier transform to determine their frequency. Next, set a high-pass filter above the frequency of the features. Lastly, the high-pass digitally filtered images were subtracted from the original image to remove artifacts of interest.

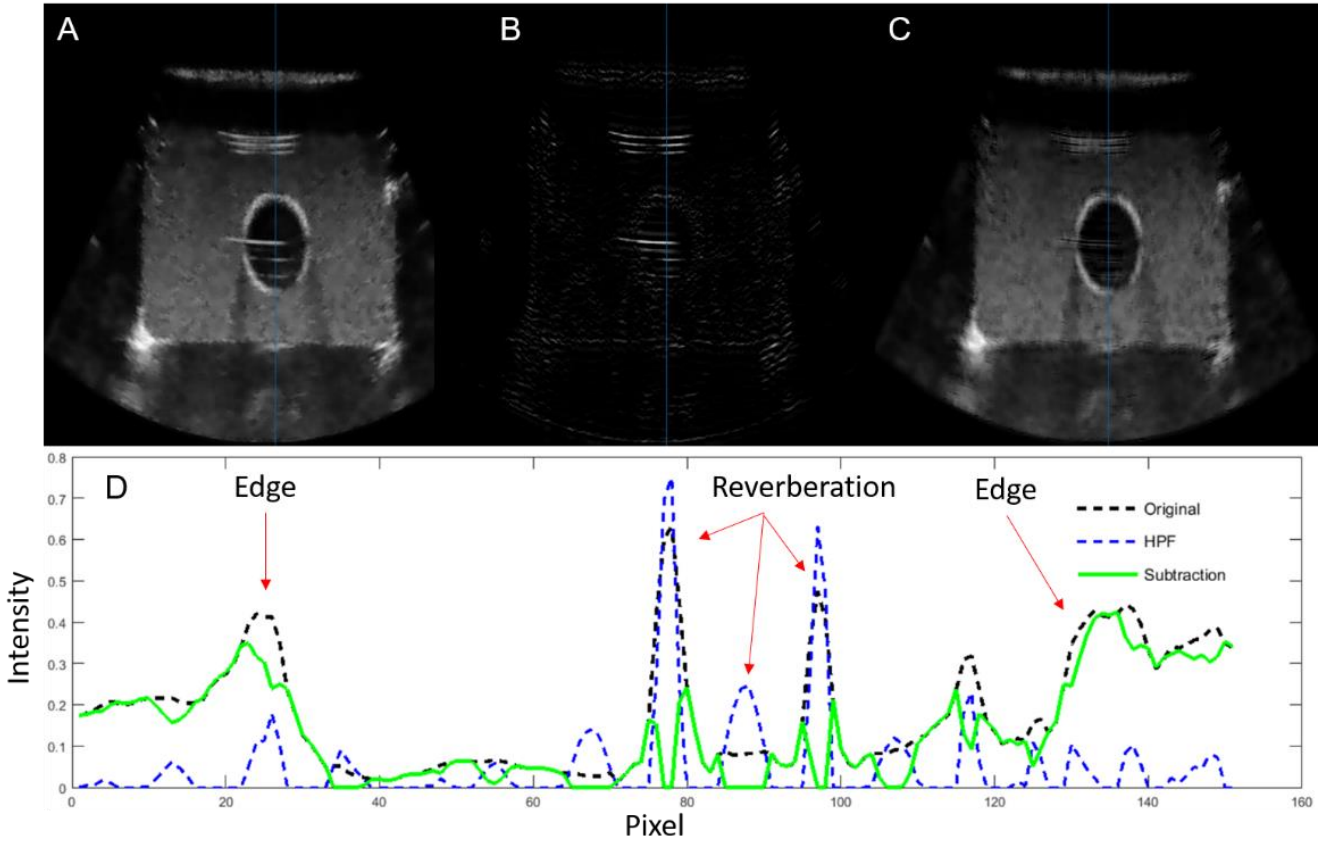

Figure A.3 Reverberation reduction. The wiener filtered (A), the high-pass filtered (B), and the stubtracted images (C) are shown. Intensity profiles (D) through the three high-frequency objects in the right center are shown.

The speed-of-sound correction algorithm is in effect a non-linear sampling problem, and with some simple assumptions, can be reversed engineered and through interpolation methods a corrected image produced. Images can be segmented (skin, soft tissue, bladder) and resampled with the appropriate speed of sound. There is exhaustive literature on speed of sound correction algorithms discussed in Chapter 3.

Refraction is a fairly complicated artifact and very difficult to correct. First, we can calculate the change in depth as a function of lateral displacement (Figure A.3) by applying Snell's law.

$$\delta x = 2 * R * \sin\left(\frac{\pi}{2}\right) * \sin(\theta_t - \theta_i) \tag{A.1}$$

$$\sin\theta_t = \frac{c_2}{c_1} * \sin(\theta_i) \tag{A.2}$$

$$\sin\theta_t = \frac{x}{R} \tag{A.3}$$

Utilizing these fundamental equations, the total propagation length and time can be calculated as a function of x, with and without refraction.

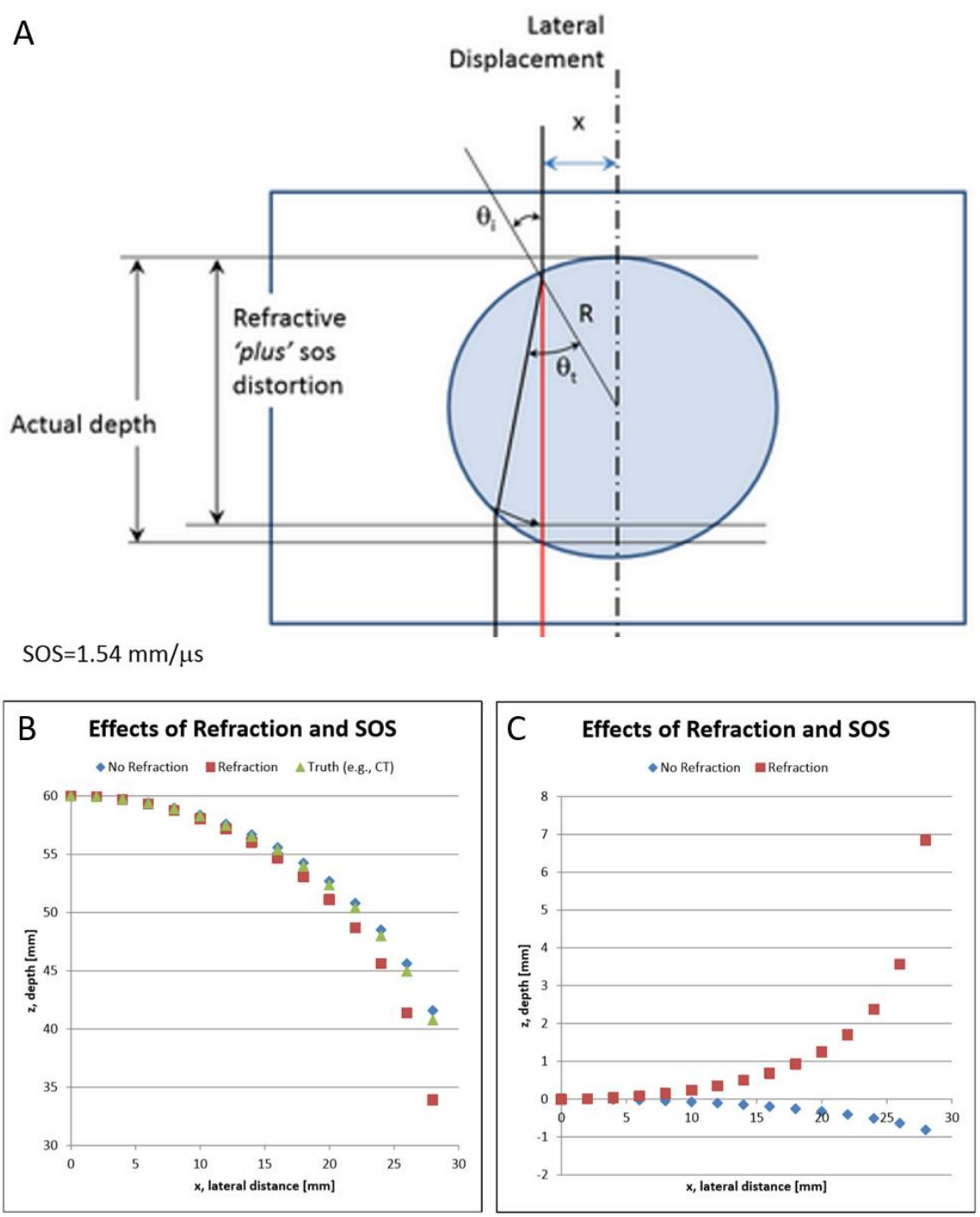

Figure A.4 Refraction quantitated. A) Refraction diagram, B) effects of refraction and SOS between depths of 30-60mm and B) 0-8 mm.

In summary, tissue heterogeneity (fat versus bladder) distorts margins by approximately 1.0 mm. The error in the lateral displacement can exceed 1 mm when the lateral distance exceeds R/2. The effect is to flatten the bladder and reduce its volume. Work with spatial compounding protocols may improve edge detection when refractive artifacts are present. In terms of the other artifacts, efforts to isolate and remove speckle and reverberation blurred the edges of the bladder and reduced the volume of the bladder when automatic edge detection methods were applied.

APPENDIX B Cytokine Data

The Canine serum 8-plex (Il-2, IL-6, IL-8, IL-10, MCP-1, TNFa & KC) cytokine assay ran without any issues. The data shown shows average concentration values of replicate wells. If the value falls outside the standard curve, this will be denoted by "OOR<" or "OOR>" (Out of Range) in this column. Extrapolated concentrations were calculated by the BioPlex software on values that are outside of the range of the standard curve. The software also calculated values for wells with negative fluorescence (fluorescence below the background fluorescence). These are marked with an asterisk.

Table B.1 Results of the Luminex bead panel. Concentrations are in [pg/ml].

	IL-10	**IL-6**	**IL-8**	**MCP-1**	**KC**
Patient 1					
PreSerum	*11.69	*3.79	13481.01	402.4	2811.43
PostSerum	41.28	*3.09	7874.49	404.13	1922.7
Day3	*16.79	*3.09	16231.3	371.74	3034.4
Patient 2					
PreSerum	55.61	*5.90	5016.12	259.92	592.41
PostSerum	60.07	*1.68	2963.01	181.05	455.68
Day3	52.28	*3.09	4394.8	331.97	541.16
FinalSerum	39.1	*3.09	4932.16	311.33	700.74
Patient 3					
PreSerum	*8.70	OOR <	7656.18	OOR <	1037.46
PostSerum	*19.90	*4.50	5035.9	OOR <	810.17
Day3	*17.30	OOR <	7298.83	OOR <	1091.74
FinalSerum	*24.09	77.59	5182	456.22	2159.41
Serum	OOR <	*5.20	6992.47	377.76	1332
control 1	*5.78	*28.39	3956.81	267.68	351.35
control 2	OOR <	*4.50	7241.35	OOR <	1197.58
control 3	178.35	*0.27	3523.75	OOR <	406.83

*Calculated values for wells with a negative fluorescence. IL-2 and TNF-α were below the detectable limit for all measurements

Patient 1 Medical History. Patient 1 is a castrated 10 year old male Golden Retriever. Patient 1 first presented to the PUVTH medical oncology department on 5/15/15 for evaluation of two fast growing masses on the right shoulder and cranial sternum. The owner noticed these two masses about 3 weeks from that date. The other masses along his body have been present for approximately two years according to the owner. Patient 1 has no history of any other medical problems. His growing masses were biopsied and it was determined that the mass on Patient 1's right shoulder was consistent with a soft tissue sarcoma (special stains were negative for histiocytic sarcoma or hemangiosarcoma) and the one on his sternum was consistent with lipoma.

Punch biopsies from both cutaneous masses were submitted for microscopic evaluation. The biopsy of soft tissue from the right shoulder contained a proliferation of atypical spindle and round cells with indistinct cell limits, moderate to abundant amphophilic cytoplasm and large round to pleomorphic nucleus with single or multiple nucleoli. There were 16 mitotic figures per 4 hpf, some atypical. More than 70% of this sample contains necrotic tissue and mixed leukocytic infiltrates in addition to septal fibrosis.

The atypical round/spindle cells with large nucleus were negative for CD18. Some foamy cells interpreted as macrophages as well as many small round cells interpreted as leukocytes were CD18 positive. The atypical cells were CD31 negative. The atypical cells were not considered to be of leukocytic or endothelial origin, leaving the diagnosis of soft tissue sarcoma unmodified to this point.

Patient 1 was taking Tramadol 50mg tablets (3 every 8-12 hours), Clavamox 375mg tablets (2 every 12 hours) and Metronidazole 500mg tablets (1 every 12 hours)

Tramadol is a synthetic opioid that helps to alleviate pain. Possible side effects include sedation, respiratory depression and GI upset. Clavamox medication is an antibiotic and is given around the time of a meal to help avoid adverse side effects, such as nausea, vomiting, diarrhea or a decrease in appetite from occurring. Metronidazole is an antibiotic for soft stools and diarrhea.

Patient 1 received only 3 out of 5 fractions. Our goal was to stabilize the size or shrink down the tumor in size for a period of time with RT, effectively control the local disease with minimal side effects. The mass has been stable in size since the beginning of RT, however there is progression on the surface of the skin, where the mass has been progressively protruding and bleeding. The mass has been growing rapidly in the 2 weeks since prescribing treatment to treatment delivery, which is consistent with a high grade tumor. Due to Patient 1's quickly degrading quality of life, it was recommended to discontinue RT and humanly euthanize.

Patient 2 Medical History. Patient 2 is a spayed female chocolate Labrador retriever, 8 years and 9 months in age. On 4/15/2015 the mass on Patient 2's right flank was first found on routine health exam at an animal clinic not affiliated with PUVTH. A fine needle aspirate/cytology revealed atypical mesenchymal cells. A biopsy of the mass was then taken on 4/20/2015 which revealed low grade nerve sheath tumor. Tumor cells extended into the margins. Mitotic index was found to be 4 per 10 HPF. On 5/28/2015 Patient 2 presented to the PUVTH for further evaluation of the tumor. On CT scan a single nodule was found on the right adrenal gland (2.1 cm x 1.5 cm). On 6/8/2015 Patient 2 presented to PUVTH for palliative RT treatment of her nerve sheath tumor and right adrenal mass. Patient 2 has been doing well at home and has been eating and

drinking well. No sneezing, coughing, diarrhea or vomiting has been observed since the last visit.

Patient 2 has been on Tramadol 50mg tablet (2 every 12 hours), Phenoxybenzamine 9mg capsule (1 every 12 hours) and Metronidazole 250mg tablet (2 every 12 hours). Phenoxybenzamine is to control blood pressure in the case the adrenal tumor is pheochromocytoma, which causes hypertension. No present side effects related to the medications.

Patient 2 received a total of 5 daily doses of 4 Gy each. Patient 2 received palliative RT for both the peripheral nerve sheath tumor, as well as right adrenal gland mass. Palliative RT is performed to stabilize or potentially shrink the tumor in size, the goal not being to cure the tumor, but to control the local disease for a time with minimum side effects. Good quality of life are very important.

Patient 3 Medical History. Patient 3 is a castrated English Springer Spaniel, 10 years and 11 months in age. Patient 3 presented to the PUVTH Radiation Oncology service for repeat evaluation of a previously irradiated nasal tumor. Patient 3 was diagnosed with a nasal tumor via CT scan in June of 2015 which could not be definitively diagnosed due to positioning and small samples. Patient 3 underwent palliative RT following this which was completed on 6/12/2015.

Patient 3 has mucus discharge coming from his left nostril and more serious discharge coming from his right nostril. No epistaxis has been seen since his previous visit. Patient 3 has seemed uncomfortable trying to sleep at night when there is a lot of discharge. He is eating and drinking well and he has not had any coughing, sneezing or GI upset.

Multiple fragments from a mass in the right nasopharynx were submitted for microscopic evaluation. Some samples consisted of normal nasal conchae, others are partially lined by pseudostratified respiratory epithelium and contain a submucosal proliferation of islands and cords of atypical polygonal cells with distinct cell limits, moderate amphophilic cytoplasm and large round nucleus with single or multiple nucleoli. Nuclear atypia was moderate with some karyomegalic cells. Abundant fibrocollagenous stroma surrounded variably sized aggregates of neoplastic cells. There were 25 mitotic figures per 10 hpf. There were extensive areas of necrosis. A set of samples consisted of haired skin with expansion of the dermis and subcutis by fibrosis and mixed infratrates of leukocytes (plasma cells, macrophages, lymphocytes and neutrophils). The inflammation extended to the adjacent skeletal muscle. Neoplastic growth was not observed in these samples.

Patient 3 was prescribed Tramadol 50 mg tablets (1.5 tablets by mouth every 8-12 hours), Prednisone 10mg tablet (1 by mouth every 24 hours), Keppra 500 mg tablet (1.5 by mouth every 8 hours) and Genteal Gel (1/4 in strip to both eyes once every 8 hours). Prednisone is a steroid medication to reduce inflammation. Keppra (aka Levetiracetam) is an anti-convulsant medication. Genteal Gel is a topical lubricant.

VITA

VITA

Education

Ph.D. Candidate, August 2016: Purdue University, School of Health Sciences.
Major: Medical Physics

Master of Science, May 2012: University of Miami, Biomedical Engineering.
Major: Medical Physics

Bachelor of Science, May 2008: Mount Saint Mary's University.
Major: Mathematics

Certifications

American Board of Radiology, Passed Part 1 in Therapeutic Radiological Physics (August 2014)

Research Experience

Graduate Research Assistant, August 2013 – present: Purdue University, Division of Medical Physics, School of Health Sciences. Advisor: Dr. Keith Stantz (kstantz@purdue.edu).

Research Projects

Thesis: Ultrasound and photoacoustic methods for anatomic and functional imaging in image guided radiation therapy

- Validating hemoglobin saturation and dissolved oxygen in tumors
- Design a platform and phantom model for ultrasonic imaging in combination with CT
- Quantify the resolution of three-dimensional ultrasound systems

Experience and Expertise

- Photoacoustic spectroscopy experiments
- Biohazard handing: blood
- Animal handling: mice and rats
- Image processing and programming: MATLAB
- Computer Aided Design: Catia, Solidworks
- Machining: Haas VF2 Mill, CNC Lathe, Laser Cutter, 3D printing

Research Assistant, 2008 – 2013: The Miami Project to Cure Paralysis, University of Miami Miller School of Medicine. Supervisor: Dr. Helen Bramlett (hbramlett@miami.edu)

Research Projects

- *In-vivo* EEG recordings, wrote software for sub-convulsive seizure detection
- *In-vitro* electro physiology experiments
- Collected and analyzed data, developed experimental protocol for stroke, seizure and simulated traumatic brain injury experiments

Clinical Experience

Medical Physics Volunteer, Graduate Student, 2008-2013¨Sylvester Comprehensive Cancer Center, University of Miami Miller School of Medicine. Advisor: Dr. Weizhao Zhao (w.zhao1@miami.edu).

- IMRT QA tests using Sun Nuclear MapCheck
- Accuray CyberKnife Treatment Planning System
- Nucletron SPOT (Intro-operative prostate brachytherapy)
- Daily, monthly and annual QA tests for linear accelerators (Varian (23ix and Trilogy)
- TrueBeam commissioning (SCCC, Deerfield Beach, FL)
- Eclipse Treatment Planning System
    - 3D-RT, IMRT, VMAT, Multimodal image registration

Masters Project: Radiographic film dosimetry: automate absolute dose verification using MATLAB

Guest Lectures

Purdue School of Health Sciences, Introduction to Medical Diagnostic Imaging (HSCI570). CT filtered back projection and ultrasound. Spring Semester, 2016

Purdue School of Health Sciences, Occupational Ergonomics (HSCI580). Radiation exposure and occupational safety. November 19, 2015.

Purdue School of Health Sciences, Seminar (HSCI696)**.** Ultrasound and photoacoustic methods for image-guided radiotherapy to treat canine urinary bladder cancer. January 13, 2015

Manuscripts

Justin T Sick, Nicholas J Rancilio, Caroline V Fulkerson, Patrick J LaPetina, Jeannie M Poulson, Deborah W Knapp, Keith M Stantz. Construction of an ultrasound guidance platform for image-guided radiotherapy with the intent to treat transitional cell carcinoma. Journal of Applied Clinical Medical Physics (*Submitted*, *May 2016*)

Justin Sick, Jenna Burnett, Ning Cao, Bo Liu, Harikrishna Nakshatri, Marc Mendonca, Keith Stantz. Validating hemoglobin saturation and dissolved oxygen in tumors using photoacoustic computed tomographic spectroscopic imaging. Journal of Applied Optics (*Draft*)

Publications

Justin Sick, Eric Bray, Amade Bregy, W. Dalton Dietrich, Helen M. Bramlett, Thomas Sick. EEGgui: A program used to detect electroencephalogram anomalies after traumatic brain injury. Source Code for Biology and Medicine (2013), 8:12

Amade Bregy, **Justin Sick**, Eric Bray, Alexandra Wick, W. Dalton Dietrich, Thomas Sick, Helen Bramlett. Subconvulsive epilepsy and changes in ptz-induced seizure threshold in rats 1 year after moderate fluid percussion brain injury. Journal of Neurotrauma (2012), 29(10):A67

Ami P. Raval, **Justin T. Sick**, Gabriel J Gonzalez, R. Anthony DeFazio, Chuanhui Dong, Thomas J. Sick. Chronic nicotine causes synaptic dysfunction in hippocampus of female rats. Neuroscience Letters (2012), 517:41-46

Zhuange Z, Yang B, Theus MH, **Sick JT**, Bethea JR, Sick TJ, Liebl DJ. EphrinBs regulate d-serine synthesis and release in astrocytes. Journal of Neuroscience (2010), 20(47):16015-24

Conference Presentations and Abstracts

Sick J, Rancilio N, Fulkerson C, LaPetina P, Poulson J, Knapp D, Stantz K. Construction of an ultrasound guidance platform for image-guided radiotherapy with the intent to treat transitional cell carcinoma. Annual Scientific Meeting of the American Association of Physicists in Medicine. Washington D.C., July 31-August 4, 2016. (Oral Presentation)

Burnett J, **Sick J*,** Cao N, Liu B, Nakshatri H, Mendoca M, Stantz K. Validating hemoglobin saturation and dissolved oxygen in tumors using photoacoustic computed tomographic spectroscopic imaging. Annual Scientific Meeting of the American Association of Physicists in Medicine. Washington D.C., July 31-August 4, 2016. (Oral Presentation, *Presenting Author)

Sick J, Rancilio N, Blake S, Heng H, Poulson J, Knapp D, Stantz K. Ultrasound guided radiation therapy of the canine urinary bladder using a custom designed image guidance platform. Spring Clinical Meeting of the American Association of Physicists in Medicine. St. Louis, MO, March 7-10, 2015. (Poster)

Sick J, Heng HG, Knapp D, Poulson JM, Stantz K., Rancilio N. Image-Guided Radiotherapy and the Use of Photoacoustic Ultrasound for Imaging the Canine Urinary Bladder: A Pilot Study. Annual Scientific Meeting of the American Association of Physicists in Medicine. Austin, TX, July 20-24, 2014. (Poster)

Jenna Burnett, **Justin Sick**, Keith Stantz. Validating hemoglobin saturation and dissolved oxygen in tumors using the OxyLab probe and photoacoustic imaging. Summer Undergraduate Research Fellowship Symposium, 2014